See-Saw Effect of Substitutional Point Defects on Electrochemical Performance in Single Crystal $LiNiO_2$ Cathodes

Leonhard Karger[a], Svetlana Korneychuk[b,c], Wessel van den Bergh[a], Sören L. Dreyer[a], Ruizhuo Zhang[a], Aleksandr Kondrakov[a,d], Jürgen Janek[a,e*], and Torsten Brezesinski[a*]

[a]Battery and Electrochemistry Laboratory (BELLA), Institute of Nanotechnology, Karlsruhe Institute of Technology (KIT), Herrmann-von-Helmholtz-Platz 1, 76344 Eggenstein-Leopoldshafen, Germany

[b]Institute of Nanotechnology, Karlsruhe Institute of Technology (KIT), Herrmann-von-Helmholtz-Platz 1, 76344 Eggenstein-Leopoldshafen, Germany

[c]Karlsruhe Nano Micro Facility (KNMFi), Karlsruhe Institute of Technology (KIT), Herrmann-von-Helmholtz-Platz 1, 76344 Eggenstein-Leopoldshafen, Germany

[d]BASF SE, Carl-Bosch-Str. 38, 67056 Ludwigshafen, Germany

[e]Institute of Physical Chemistry & Center for Materials Research (ZfM/LaMa), Justus-Liebig-University Giessen, Heinrich-Buff-Ring 17, 35392 Giessen, Germany

*Email: juergen.janek@kit.edu, torsten.brezesinski@kit.edu

Abstract

Layered oxide cathode materials, such as $LiNi_aCo_bMn_cO_2$ or $LiNi_aCo_bAl_cO_2$, are sought after mainly because of their high theoretical specific capacity. Especially those with a high nickel content are being pursued to increase capacity and lower costs. In these materials, substitutional defects are a common feature and typically associated with poor overall quality. Herein, we employ a sodium to lithium ion exchange to produce $LiNiO_2$ (LNO) without such characteristic defects. Three different methods are used to tailor the primary particle (grain) size over a broad range, and each material is subjected to electrochemical testing. By analyzing the initial charge-discharge profiles, we separate kinetic hindrance and structural degradation as two independent contributions to the first-cycle capacity loss. We find that $Ni_{Li}^{\bullet}$ point defects stabilize LNO at high potentials and help mitigate material degradation while leading to incomplete discharge. The kinetic hindrance at the end of discharge vanishes upon their removal, but the degradation at high states of charge becomes more pronounced. We examine the cause of material degradation and corroborate the results by artificially introducing pillaring Mg^{2+} ions through a novel dual-ion exchange as a model system for nickel substitutional defects. This methodology may be exploited to identify an optimal concentration of pillar ions, especially in a range of defect densities that is inaccessible by conventional solid-state synthesis.

Introduction

Substitutional defects are present in cathode materials of the $LiNi_aCo_bMn_cO_2$ (NCM or NMC) and $LiNi_aCo_bAl_cO_2$ (NCA) solid solutions.[1–3] Especially the 100% nickel endmember, $LiNiO_2$ (LNO), is prone to off-stoichiometry, which strongly affects its electrochemical behavior.[4] Typically, LNO is made through solid-state synthesis in an oxygen atmosphere at high temperatures. This thermal process leads to an inherently "lithium deficient" or "off-stoichiometric" LNO of the general formula $Li_{1-z}Ni_{1+z}O_2$.[4–6] Depending on the relative ratio of nickel to lithium, as well as the calcination temperature, different types of defects can emerge. For example, Ni/Li antisite defects, which refer to $\mathrm{Li}_{\mathrm{Ni}}''$ and $\mathrm{Ni}_{\mathrm{Li}}^{\bullet\bullet}$ point defects (Kroeger-Vink notation), are only observed for large off-stoichiometries of $z \geq 0.15$.[7] For the close-to-stoichiometric LNO, which is the material of interest for lithium-ion battery (LIB) application, only $\mathrm{Ni}_{\mathrm{Li}}^{\bullet}$ defects, accompanied by $\mathrm{Ni}_{\mathrm{Ni}}'$ for charge compensation, are the prevailing defects and should be considered for understanding the electrochemistry of LNO.[7] In the context of this study, for simplicity, we only mention the $\mathrm{Ni}_{\mathrm{Li}}^{\bullet}$ defects when referring to the combination of $\mathrm{Ni}_{\mathrm{Li}}^{\bullet}$ and $\mathrm{Ni}_{\mathrm{Ni}}'$.[2] Note that these substitutional defects are a result of both incomplete oxidation of Ni^{2+} to Ni^{3+} and the similar ionic radii of Ni^{2+} and Li^{+}, and are as such inherent to LNO prepared by solid-state synthesis.[8–10]

Optimized calcination protocols and careful stoichiometric control can achieve defect concentrations of no lower than 1.6 mol% of $\mathrm{Ni}_{\mathrm{Li}}^{\bullet}$ with respect to nickel.[11,12] Furthermore, only the annealing step seems to be crucial for the fraction of $\mathrm{Ni}_{\mathrm{Li}}^{\bullet}$, as no signs of nickel migration in the bulk are found during cycling in the stable electrochemical window of LNO in recent studies, although this is still a subject of debate.[10,13] This is not least caused by the experimentally challenging characterization and quantification of point defects. Common ways to probe $\mathrm{Ni}_{\mathrm{Li}}^{\bullet}$ are a combination of powder X-ray (PXRD) and neutron diffraction (ND), magic-angle spinning nuclear magnetic resonance (MAS NMR) spectroscopy, and magnetometry.[4,12,14]

Achieving a low $\mathrm{Ni}_{\mathrm{Li}}^{\bullet}$ defect density is considered desirable, as the specific charge and discharge capacities increase due to facilitated lithium diffusion, but other effects have been reported, too.[15] Increasing the fraction of nickel substitutional defects increases the potential at which the so-called H3 phase forms (the last reversible transition during the LNO charge/discharge).[12] When going beyond this transition, the H4 phase forms, which is associated with oxygen release and irreversibility.[16,17] High defect concentrations of ≥ 7.2 mol% suppress this phase transition completely, which may be indicative of the stabilizing properties of $\mathrm{Ni}_{\mathrm{Li}}^{\bullet}$ defects.[18] Another aspect is their relation to the first-cycle capacity loss, as reported by Arai *et al*., Delmas *et al*., and Bianchi *et al*. In particular, they emphasized the need of lowering the defect density for decreasing first-cycle loss.[19–21] Subsequent studies did not find this correlation and instead proposed a direct link between first-cycle loss and primary particle size of the active material.[11,12,22] However, since $\mathrm{Ni}_{\mathrm{Li}}^{\bullet}$ defects affect the lithium transport properties through vacancy trapping and by acting as a diffusion barrier, it is difficult to distinguish

between the influence of point defects and size effects, which arise at different calcination temperatures.[23] This intrinsic convolution of particle size and defect density contributions to the electrochemical performance demand further study, as particularly for single-crystalline morphologies diffusion-induced capacity loss can be substantial.[22,24]

Recently, we have developed a method to prepare LNO that is free of $Ni_{Li}^{\bullet}$ defects by synthesizing perfectly layered $NaNiO_2$ (NNO) and then conducting sodium to lithium ion exchange in molten salts (yielding ion-exchanged LNO, referred to as IE-LNO).[14] In this study, we report on the particle-size-dependent electrochemistry of single crystal IE-LNO cathodes and correlate capacity loss and stability to grain (primary particle) size and $Ni_{Li}^{\bullet}$ defects being present or absent. We stress the ambivalent character of $Ni_{Li}^{\bullet}$ defects, which act similarly to (stabilizing) pillar ions but impede the lithium diffusion at the same time. Upon their removal, these effects are reversed. This means that the charge transport improves while material stability decreases, tilting the see-saw-like behavior to the other extreme.

Results and Discussion

Optimization of LNO Synthesis

Solid-state synthesis of NNO leads to single-crystalline particles with uniform distribution of sodium and nickel, as can be seen from the scanning transmission electron microscopy (STEM) image and energy dispersive X-ray spectroscopy (EDS) maps in **Figure 1a**-**c**. High-resolution TEM (HRTEM) imaging of focused ion beam (FIB) cross sections indicates that there is little strain or bending of individual nickel oxide slabs in the as-made NNO (**Figure 1d**) and the surface is covered by an amorphous layer, likely residual NaOH (**Figure 1e**). When this material is subjected to ion exchange and washed with water, the overall morphology is retained, but the internal structure exhibits abundant intragranular cracks and domains of high sodium content (**Figure 1f**-**j**). These sodium-rich domains may be caused by sluggish diffusion because of crack formation or inhibition of ion exchange at the lithium-rich surface.

As shown in our preceding work, post-annealing of the IE-LNO at elevated temperatures produces a material with ≥ 5 mol% $Ni_{Li}^{\bullet}$ defects, which seems to be due to sodium diffusing out of the structure and being replaced by Ni^{2+}. For this reason, it was tested whether additional lithium can prevent structural degradation upon heating in order to preserve a low- or ideally zero-defect state. To this end, the IE-LNO was combined with 10 mol% $LiOH{\cdot}H_2O$ and annealed at 700 °C for 6 h (referred to as IE-LNO+LiOH-6h). Rietveld analysis of PXRD data collected from this material reveals a defect concentration of 2.5(3) mol% $Ni_{Li}^{\bullet}$ (**Table 1**). When the material is annealed at the same temperature for 40 h (referred to as IE-LNO+LiOH-40h), a decrease in defect concentration to 1.6(2) mol% is observed, which is comparable to that of the polycrystalline reference LNO (referred to as PC-LNO). Electron microscopy images of this annealed material indicate the presence of rhombohedral voids (**Figure 1k**-**o**), containing sodium on their inner surfaces. Apparently, the cracks heal out and

rearrange to form said voids, and the residual sodium diffuses toward the surfaces, where it is deposited as an oxide. In the remaining bulk structure, no sodium is detected by EDS. Therefore, annealing seems to be effective at removing sodium from the layered phase, but it also leads to the formation of voids and $Ni_{Li}^{\bullet}$ defects. The voids are believed to still hinder lithium diffusion, similar to the cracks that are present prior to heating. In addition, post-annealing re-introduces point defects and is therefore not suited for retaining the initially $Ni_{Li}^{\bullet}$-free nature. Instead, sodium should be removed completely in a temperature range where substitutional defects do not form. Nevertheless, the IE-LNO+LiOH-40h material exhibits improved capacity over IE-LNO annealed in the absence of $LiOH \cdot H_2O$ (**Figure S1**, Supporting Information).

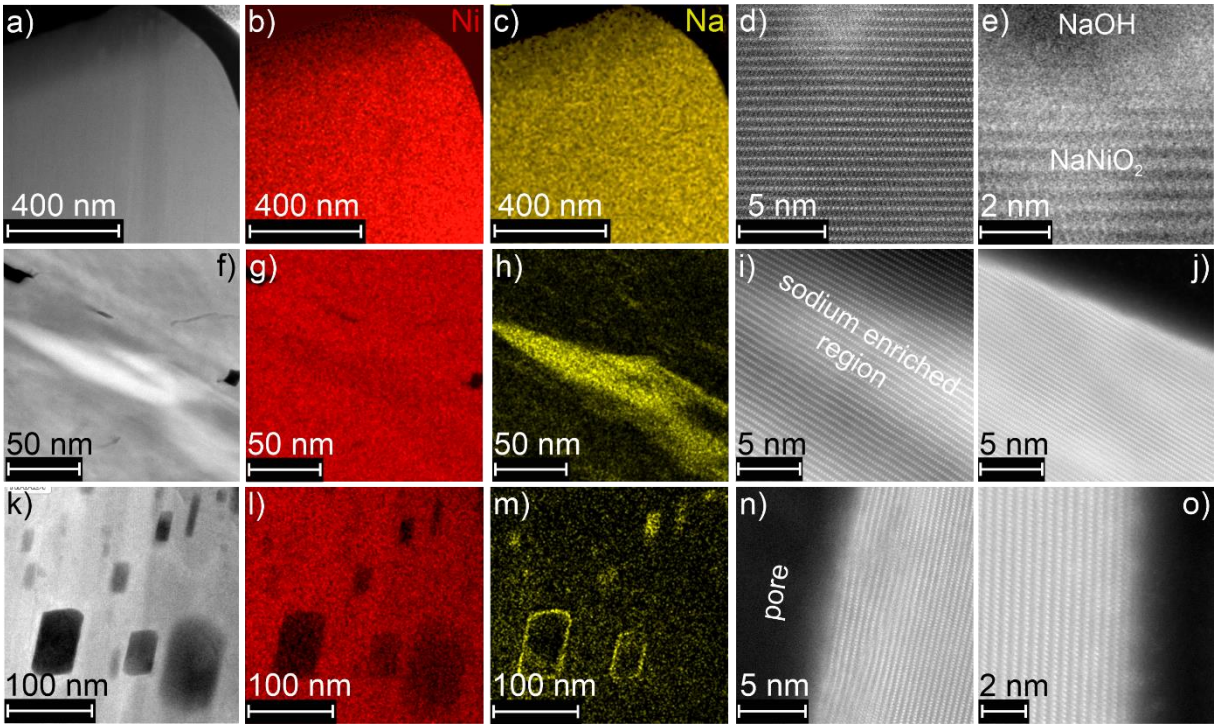

Figure 1. (a) STEM and (b,c) EDS results for FIB-cut NNO. HRTEM of (d) NNO bulk and (e) particle edge. (f) TEM and (g,h) EDS results for FIB-cut IE-LNO. HRTEM of (i) IE-LNO bulk and (j) particle edge. (k) TEM and (l,m) EDS results for FIB-cut IE-LNO+LiOH-40h. HRTEM of (n) IE-LNO+LiOH-40h bulk and (o) particle edge.

Table 1. Results from Rietveld analysis of the PC-LNO and IE-LNO samples before and after annealing in the presence of $LiOH \cdot H_2O$.

Sample	R_{wp} [%]	R_{Bragg} [%]	a [Å]	c [Å]	V [Å^3]	Defects [mol%]
PC-LNO	11.0	2.1	2.8733(1)	14.1854(6)	101.42(1)	$Ni_{Li}^{\bullet}$ 1.7(2)
IE-LNO	11.5	1.8	2.8746(6)	14.1968(54)	101.70(2)	$Ni_{Li}^{\bullet}$ 0 $Na_{Li}^{\times}$ 5.0(8)*
IE-LNO+LiOH-6h	15.6	2.0	2.8758(1)	14.1781(12)	101.55(1)	$Ni_{Li}^{\bullet}$ 2.5(3)
IE-LNO+LiOH-40h	10.3	1.7	2.8750(1)	14.1765(12)	101.48(1)	$Ni_{Li}^{\bullet}$ 1.6(2)

*From PXRD and NMR spectroscopy[14]

A promising strategy to avoid the aforementioned problem of incomplete ion exchange is the application of sufficiently small crystallites that allow for short sodium diffusion path lengths. Control over the NNO particle (grain) size can be achieved by varying the annealing temperature in the range of 450-750 °C.[14] Furthermore, using NaOH instead of Na_2O_2 as precursor (sodium source) leads to a decrease in primary particle size.

Temperature-Based Particle Size Tailoring

A series of NNO samples with different particle sizes was synthesized by heating NaOH with $Ni(OH)_2$ at 450, 600, and 700 °C, as well as by heating NiO nanoparticles with Na_2O_2 at 750 °C (referred to as NNO-ϑ, with ϑ being the temperature). These NNO samples were then subjected to ion exchange (referred to as IE-LNO-ϑ; see Experimental section for details). As can be seen from the scanning electron microscopy (SEM) images in **Figure 2a**-**d**, the particle size increases with increasing temperature. The size distribution is relatively broad, with d_{50} values ranging from 480 nm for IE-LNO-450 to 6.67 µm for IE-LNO-750 (**Figure 2e**). With regards to faceting, no obvious correlation to the particle shape is apparent, even though they are not completely spherical. After ion exchange, the crystallites appear to be well separated, and virtually no agglomeration of the monolithic particles is observed. As expected, the materials crystallize in the *R*−3*m* space group, and Rietveld analysis reveals similar lattice parameters for all samples (**Table 2**), in good agreement with literature results.[6] Therefore, we assert that the particles are of single-phase nature. However, particularly the larger particles may still contain residual sodium, as is evident from the decrease of $Na_{Li}^{\times}$ to 0 mol% with decreasing particle size. This is confirmed by EDS measurements conducted on IE-LNO-700; small particles do not contain sodium, but larger particles exhibit the sodium-rich domains described above (**Figure S2**, Supporting Information). The evolution of lattice parameters corroborates this finding, with decreasing values for *a* and *V* with decreasing grain size. IE-LNO-750 shows a smaller *c*-parameter, which might be related to the different (more oxidizing) sodium

precursor used in the synthesis. Nevertheless, a clear trend of increasing cell volume and lattice parameters with increasing temperature is found for the parent NNO samples (**Table S1**, Supporting Information). Overall, controlling the annealing temperature yields the desired materials, namely a size-tailored IE-LNO series.

The IE-LNO samples were then subjected to electrochemical testing at C/10 rate in LIB half-cells (3.0-4.3 V vs. Li^+/Li). As is shown in **Figure 2f**-**i**, the first-cycle specific discharge capacities are rather low, with the highest achieved with IE-LNO-700 and IE-LNO-450 with q_{dis} = 173 and 152 mAh/g_{LNO}, respectively. No clear trend between particle size and capacity is found. However, the first-cycle capacity loss does show a distinct trend and decreases from about 31 to 8% with decreasing particle size. Furthermore, the differential capacity curves for the second cycle in **Figure 2j**-**m** reveal differences for the different IE-LNO samples. The observed dq/dV peaks have been previously assigned to structural transitions that are well known for LNO produced by solid-state synthesis.[14,25–28] In short, when charging the material, a peak that is associated with high diffusivity or small particle size (strongly dependent on the lithium intercalation at the end of discharge; in a region of the discharge profile where lithium diffusion is hindered), commonly referred to as kinetic hindrance (KH), is observed first.[29,30] The following peaks are typically labeled as H1-M, M-H2, and H2-H3, as shown in **Figure 2k**. The largest particles (IE-LNO-750) exhibit a high overpotential, and the phase transitions appear broadened when compared to IE-LNO-700. Upon moving to smaller particle sizes, the high-voltage transitions, M-H2 and H2-H3, become less intense, broadened, and shift outside the operating potential window. Also, the onset of the H3-H2 transition during discharge shifts to lower potentials with decreasing particle size, while the other peaks do not show a similar shift. By the same token, the low-voltage peaks, especially the KH peak, become more pronounced. This could be the reason why the first-cycle loss decreases with decreasing particle size, as the re-lithiation of the material becomes more effective. At the same time, these smaller particles cannot be fully charged due to voltage hysteresis, which is increased at high states of charge (high degrees of delithiation) and has been linked to surface densification.[13] Indeed, if the cells are operated at 4.8 V vs. Li^+/Li, the specific discharge capacity increases significantly, e.g., from q_{dis} = 152 mAh/g_{LNO} to 191 mAh/g_{LNO} for IE-LNO-450 (**Figure S3**, Supporting Information). Also, the smaller particles are likely to undergo more side reactions (surface degradation) due to their higher relative surface area.[31] For example, the particles need to be subjected to water washing in order to get rid of the salt used for ion exchange, which is known to cause lithium to proton exchange and subsequent formation of surface impurities, potentially lowering the fraction of active material.[32] In essence, two counteracting effects are observed in IE-LNO: (i) Destabilization of high states of charge and (ii) faster diffusion and therefore improved capacity retention in the first cycle when moving to smaller particles. One can visualize these opposing effects as the two sides of a see-saw, with optimal balance of both resulting in minimal first-cycle capacity loss.

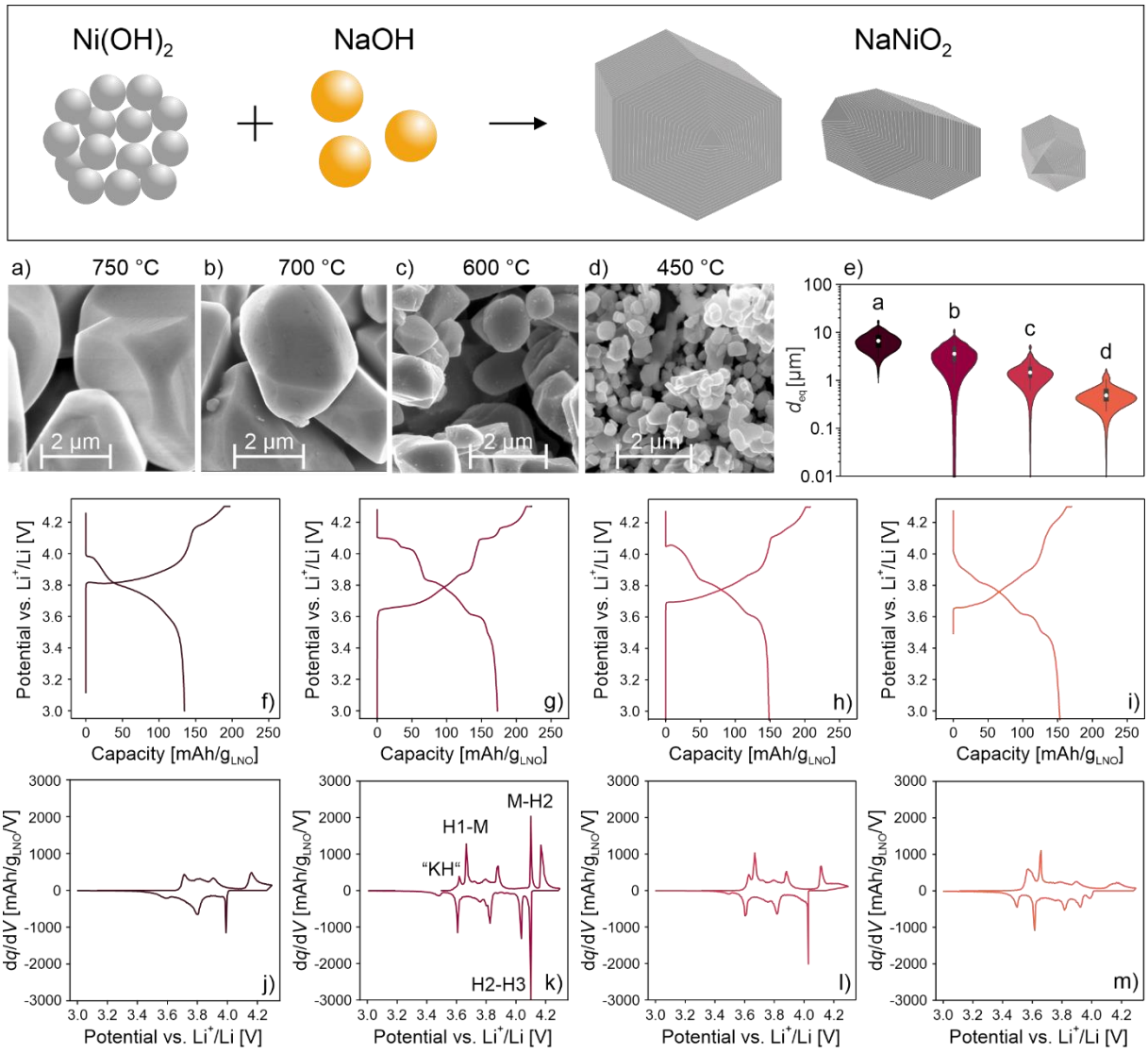

Figure 2. Analysis of temperature-based size tailoring of IE-LNO. SEM images of (a) IE-LNO-750, (b) IE-LNO-700, (c) IE-LNO-600, and (d) IE-LNO-450. (e) Corresponding particle size distribution. (f-i) First-cycle charge/discharge and (j-m) second-cycle differential capacity curves at C/10 rate (3.0-4.3 V vs. Li^+/Li). The electrochemical data are in the same order as in panels (a-d).

Table 2. Results from Rietveld analysis of the temperature-based, size-tailored IE-LNO samples.

Sample	R_{wp} [%]	R_{Bragg} [%]	*a* [Å]	*c* [Å]	*V* [Å^3]	$Na_{Li}^{\times}$ [mol%]
IE-LNO-450	15.7	4.3	2.8731(12)	14.1876(90)	101.42(12)	0
IE-LNO-600	14.9	4.8	2.8747(9)	14.1854(30)	101.51(3)	0.7(2)
IE-LNO-700	11.5	1.8	2.8746(6)	14.1968(54)	101.70(2)	5.0(8)
IE-LNO-750	14.0	3.2	2.8816(6)	14.1647(41)	101.86(2)	7.8(8)

Ball-Milling-Assisted Particle Size Tailoring

To test whether the effects observed with the temperature-based size control are of a more general nature, two other methods for tailoring the grain size of the parent NNO phase were applied. One of these is high-energy milling. Ball milling is an effective method to decrease particle size, with higher energy input and longer milling times leading to smaller particles. We specifically focused on the largest NNO particles, namely NNO-750. The latter material was milled at 300, 400, and 600 rpm for 10 min, and the as-made powders were then subjected to ion exchange (products are referred to as IE-LNO-Xrpm). With increasing rotational speed, particles with sizes ranging from d_{50} = 1.64 µm for IE-LNO-300rpm to 268 nm for IE-LNO-600rpm are obtained, as shown in **Figure 3a**-**d**. The size distributions are broader than those of the IE-LNO-ϑ samples. Already after milling at 300 rpm, nanoscale particles are present, which likely originate from chipping of the NNO-750, while the large particles remain mostly intact. This is also visible from the size analysis in **Figure 3d**, revealing a broad tail toward very small particles. Furthermore, the larger particles appear to be partially cracked, thus evidencing high mechanical stress. Structural analysis confirms all ion-exchanged materials to conform to the *R*−3*m* space group. We find increased *c*-parameter values and decreased $\mathrm{Na}_{\mathrm{Li}}^{\times}$ defect concentrations for the ball-milled materials (**Table 3**). However, even for the smallest particles, IE-LNO-600rpm, substitutional defects are observed by PXRD. The presence of sodium is further corroborated by EDS (**Figure S2**, Supporting Information). The latter could be the result of severe damage to the layered structure, leading to sodium trapping within the bulk. Indeed, the particle core of IE-LNO-600rpm is found by STEM to be non-uniform.

The materials were also electrochemically tested in LIB half-cells at C/10 rate. As mentioned above, IE-LNO-750 exhibits poor performance, which is due in part to the presence of large particles and high overpotential. Upon decreasing the particle size by milling, the specific charge and discharge capacities increase. Furthermore, the first-cycle capacity loss decreases from about 31 to 12% (**Figure 3e**-**g**), similar to the observations made for the temperature-based size tailoring. The re-lithiation is rendered more effective with decreasing particle size (i.e., the KH peak intensity increases with decreasing particle size). However, as for the high-voltage region, no clear trend is observed with these samples, as the M-H2 and H2-H3 transitions appear broadened and are partially shifted outside the potential window (**Figure 3h**-**j**). Overall, the results point to better cycling of the smaller particles, which is likely due to improved diffusion during ion exchange and battery operation. While being effective at reducing the overall grain size, ball milling does not seem promising for obtaining narrow size ranges of particles. Apart from that, sodium remains trapped within the structure irrespective of the grain size, likely due to some loss of long-range order because of mechanically introduced disorder. This in turn reduces the specific capacity to such an extent that this method was not pursued further.

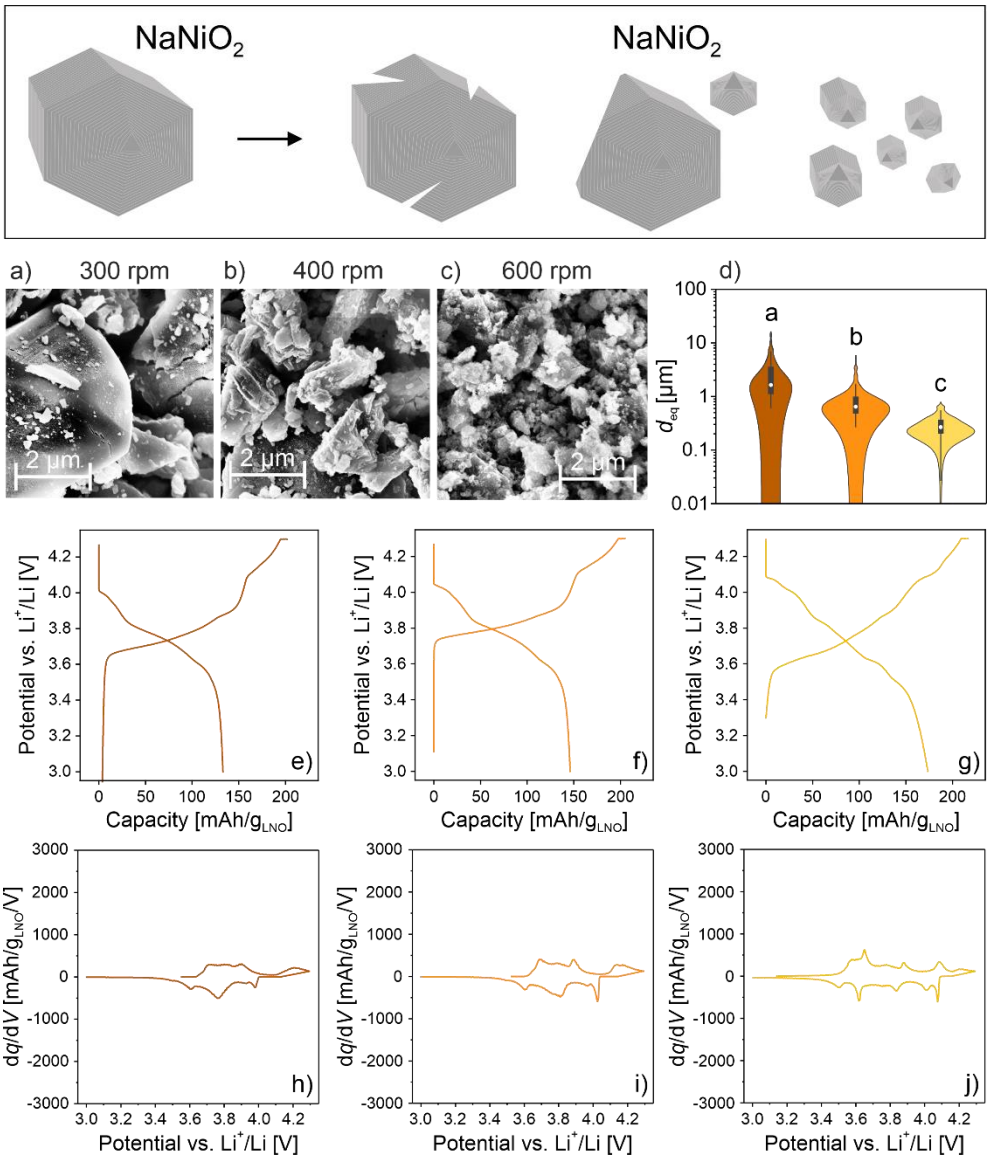

Figure 3. Analysis of ball-milling-assisted size tailoring of IE-LNO. SEM images of (a) IE-LNO-300rpm, (b) IE-LNO-400rpm, and (c) IE-LNO-600rpm. (d) Corresponding particle size distribution. (e-g) First-cycle charge/discharge and (h-j) second-cycle differential capacity curves at C/10 rate (3.0-4.3 V vs. Li^+/Li). The electrochemical data are in the same order as in panels (a-c).

Table 3. Results from Rietveld analysis of the ball-milling-assisted, size-tailored IE-LNO samples.

Sample	R_{wp} [%]	R_{Bragg} [%]	*a* [Å]	*c* [Å]	*V* [Å^3]	$Na_{Li}^{\times}$ [mol%]
IE-LNO-300rpm	14.8	2.9	2.8746(9)	14.2166(90)	101.740(96)	0.1(4)
IE-LNO-400rpm	15.3	3.6	2.8761(4)	14.2075(90)	101.78(4)	0.6(2)
IE-LNO-600rpm	15.1	3.4	2.8805(12)	14.2215(120)	102.193(120)	2.8(6)

Anti-Sintering Particle Size Tailoring

The third method to tailor particle size relies on controlling the sintering of the NNO grains during calcination. For LNO, ammonium paratungstate (APT) addition has been shown to prevent growth by acting as an anti-sintering agent.[33] Inspired by this finding, we tested whether a similar growth inhibition would be observed in the preparation of NNO. To this end, syntheses with 0.1, 0.5, 1.0, and 2.0 mol% tungsten from APT were performed and the as-made materials probed using PXRD. All samples conform to the monoclinic structure of NNO (*C*2/*m* space group), with minor differences in cell volume and lattice parameters among them (**Table S1**, Supporting Information). Note that larger differences would be indicative of tungsten inclusion. However, small amounts of rock-salt-type NiO are observed, except for the sample containing 0.5 mol% tungsten, which likely originates from experimental variation during calcination (**Figure S4**, Supporting Information). Additionally, WO_3 residues are detected for the sample containing 2 mol% tungsten. The NNO particles were also subjected to ion exchange, and the resulting materials (**Figure 4a**-**d**) are referred to as IE-LNO-YW hereafter (Y being the nominal mol% of tungsten from APT with respect to nickel). Structural analysis by Rietveld refinement suggests that all products are phase pure LNO (**Table 4**). Yet, they still contain NiO impurities, as they are carried over from the respective NNO materials. For the smaller particles, the presence of $Na_{Li}^{\times}$ defects is also apparent, while inductively coupled plasma-optical emission spectroscopy (ICP-OES) reveals a decreasing trend in the overall sodium content with decreasing particle size (**Table 4**), similar to the temperature-based size tailoring. Therefore, the higher $Na_{Li}^{\times}$ concentration seen for the smallest particles is likely caused by the rock-salt-type NiO (or partially decomposed LNO), which forms because of the increase in specific surface area (higher tungsten content) combined with water washing and drying and can be misinterpreted in Rietveld analysis as excess electron density in the lithium slab. The smaller particles also give rise to broader and less intense reflections, a sign of their nanoscale nature and/or presence of strain, rendering pattern refinements more challenging. The particle size is found to be similar for the IE-LNO-1.0W and IE-LNO-2.0W samples, with d_{50} = 191 and 226 nm, respectively (**Figure 4e**). Hence, APT addition of 1.0 mol% is sufficient to prevent sintering of the NNO grains. ICP-OES measurements also reveal the presence of tungsten in the samples, yet in lower levels than nominally used. This could be related to tungsten being located on the particle surface from which it can be removed, especially during water washing, if soluble or readily suspendable species are present.

Eventually, the IE-LNO-YW cathode materials were cycled in LIB half-cells. A similar trend to that observed with the temperature-based and ball-milling-assisted, size-tailored samples is found. With decreasing particle size, the capacity increases (**Figure 4f**-**i**). IE-LNO-1.0W delivers the highest first-cycle specific discharge capacity of q_{dis} = 186 mAh/g_{LNO}. Again, the KH region becomes more pronounced and the high-voltage transitions are muted with decreasing particle size (**Figure 4j**-**m**), perfectly following the trends outlined by the size-tailoring methods described above.

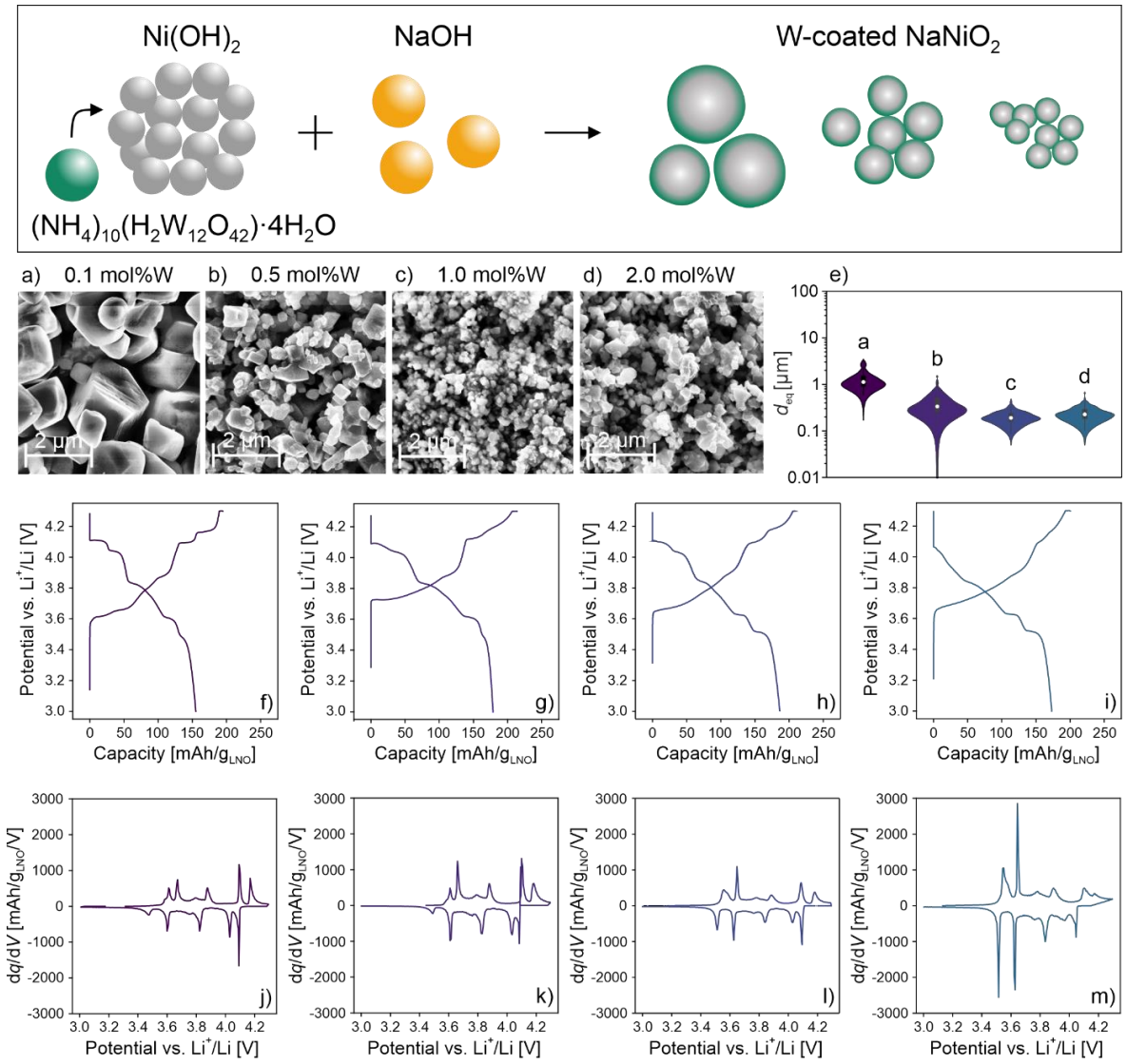

Figure 4. Analysis of anti-sintering size tailoring of IE-LNO. SEM images of (a) IE-LNO-0.1W, (b) IE-LNO-0.5W, (c) IE-LNO-1.0W, and (d) IE-LNO-2.0W. (e) Corresponding particle size distribution. (f-i) First-cycle charge/discharge and (j-m) second-cycle differential capacity curves at C/10 rate (3.0-4.3 V vs. Li^+/Li). The electrochemical data are in the same order as in panels (a-d).

Table 4. Results from Rietveld analysis and ICP-OES of the anti-sintering, size-tailored IE-LNO samples.

Sample	R_{wp} [%]	R_{Bragg} [%]	*a* [Å]	*c* [Å]	*V* [Å^3]	$Na_{Li}^{\times}$ [mol%]
IE-LNO-0.1W	15.2	3.4	2.8750(12)	14.2009(120)	101.65(12)	0.6(7)
IE-LNO-0.5W	17.7	4.7	2.8760(6)	14.1889(66)	101.65(7)	0
IE-LNO-1.0W	14.9	3.5	2.8766(4)	14.2012(41)	101.77(2)	1.8(10)
IE-LNO-2.0W	16.3	3.7	2.8775(12)	14.1768(156)	101.65(15)	2.4(21)

Sample	Li [%]	Na [%]	Ni [%]	W [%]	O [%]
IE-LNO-0.1W	95.2	3.1	100	0.07	215.2
IE-LNO-0.5W	108.7	2.6	100	0.25	261.4
IE-LNO-1.0W	0.82	2.1	100	0.43	206.3
IE-LNO-2.0W	93.1	1.2	100	0.40	208.5

When the tungsten source is added after the pre-annealing step during the NNO synthesis, a different particle morphology is obtained than with tungsten addition to the initial hydroxide precursor mixture prior to heating. After ion exchange, the primary particle agglomerates (secondary particle morphology) remain mostly intact, as shown in **Figure 5a**. For that reason, the resulting material is referred to as polycrystalline IE-LNO (here, IE-LNO-2.0W-PC). PXRD analysis of this sample reveals the presence of trace amounts of WO_3 impurities (**Figure S4**, Supporting Information). However, the main phase crystallizes in the *R*−3*m* space group; the refined lattice parameters and results from ICP-OES are given in **Table 5**. The size distribution of the primary particles, which are visible on the surface of the secondary particles, is similar to that of IE-LNO-2.0W, although some larger grains can be observed and the median size decreases from d_{50} = 226 to 166 nm (**Figure 5b**). The STEM/EDS results in **Figure 5e**-**g** indicate that the interior of the secondary particles also consists primarily of nanoscale grains. As can be seen from the mapping results in **Figure 5h**-**k**, no clear accumulation of tungsten at the grain boundaries is found. In HRTEM (**Figure 5l** and **n**) of the areas marked in **Figure 5m**, a well-layered structure without strain in the nickel slabs and the presence of minor amounts of rock-salt-type NiO toward the particle surface are evident.

Interestingly, this material is capable of delivering much higher capacities than the single-crystalline particles (**Figure 5c**). A first-cycle specific discharge capacity of q_{dis} = 204 mAh/g_{LNO} is achieved with the IE-LNO-2.0W-PC, compared to 172 mAh/g_{LNO} for IE-LNO-2.0W and 186 mAh/g_{LNO} for IE-LNO-1.0W. The preservation of the secondary particle morphology seems to help protect the IE-LNO (free) surface from degradation during ion exchange, washing, and cycling. The corresponding differential capacity curve (**Figure 5d**) reveals the same transitions observed in the IE-LNO materials discussed previously. The peak ratios closely resemble those of IE-LNO-1.0W and IE-

LNO-2.0W while showing distinct features in the KH and high-voltage regions. Consequently, this route represents the best way for preparing a competitive material and was further used in a comparison with PC-LNO.

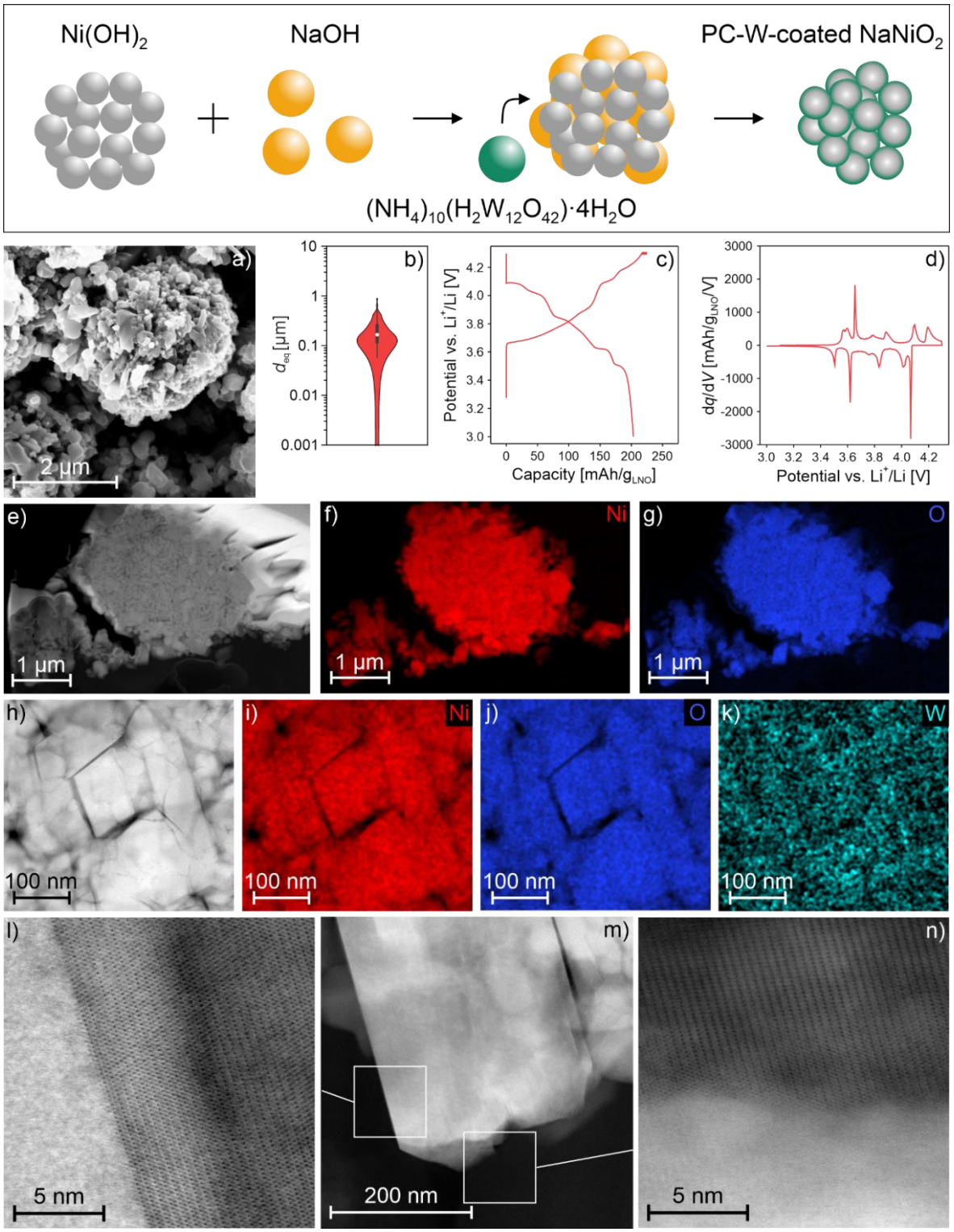

Figure 5. Structural and electrochemical analysis of IE-LNO-2.0W-PC. (a) SEM image, (b) particle size distribution, and (c) first-cycle charge/discharge and (d) second-cycle differential capacity curves at C/10 rate (3.0-4.3 V vs. Li^+/Li). (e-k) STEM/EDS results. (l,n) HRTEM of the particle edges [parallel (l) and perpendicular (n) to the layering direction], with the respective areas indicated in the STEM image in panel (m).

Table 5. Results from Le Bail analysis and ICP-OES of the IE-LNO-2.0W-PC and IE-LNO-2.0W-PC-Mg samples.

Sample	R_{wp} [%]	R_{Bragg} [%]	*a* [Å]	*c* [Å]	*V* [Å^3]
IE-LNO-2.0W-PC	16.9	3.8	2.8734(2)	14.1677(300)	101.31(24)
IE-LNO-2.0W-PC-Mg	18.2	3.7	2.8790(15)	14.1943(810)	101.887(162)

Sample	Li [%]	Na [%]	Mg [%]	Ni [%]	W [%]	O [%]
IE-LNO-2.0W-PC	92.8	2.1	-	100	0.38	211.5
IE-LNO-2.0W-PC-Mg	91.0	0.4	1.49	100	0.41	201.5

In summary, three different particle-size-tailoring methods were tested to gain insight into the electrochemistry of $Ni_{Li}^{\bullet}$-free LNO particles. All of them generated phase pure IE-LNO materials, with minor amounts of rock-salt-type NiO for the tungsten-based, anti-sintering approach. The specific capacities differ substantially among the samples from the different methods, but within each set clear size trends are observed. The reasons for the differences in performance are described above. In short, even the smallest temperature-tailored particles, IE-LNO-450 (d_{50} = 480 nm), are much larger in size than the smallest particles from the other two series, namely IE-LNO-600rpm and IE-LNO-1.0W with d_{50} = 268 and 191 nm, respectively. The best performance in all IE-LNOs is achieved with IE-LNO-2.0W-PC, which exhibits the smallest primary particle size (d_{50} = 166 nm) and benefits from a secondary particle morphology.

Individual Contributions to First-Cycle Capacity Loss

To further study the effect of the particle size on electrochemical performance, the relative capacity loss on the initial cycle, commonly known as first-cycle loss, was examined in some more detail. The corresponding results are shown in **Figure 6a**. A correlation between grain size and first-cycle loss is found for all size-tailoring methods, and an even closer correlation is observed within each set of samples. For the temperature-tailored materials, the lowest loss at a given particle size is found, while the relative losses are similar for ball milling and anti-sintering. This could be related to surface degradation upon milling and tungsten addition, which negatively affects diffusion (charge transport) in these particles. To determine the individual contributions to the first-cycle loss, a separation of capacity loss from KH at low potentials versus that at high states of charge was attempted. To this end, the charge curves were aligned in what we deem a non-critical region of good stability and maximum diffusion, namely the monoclinic phase at ~4.0 V during charge and ~3.9 V during discharge (**Figure S5**, Supporting Information). This allows separating contributions to the first-cycle loss from features above and below 3.9 V, which we assume can be attributed to KH at < 3.9 V and structural degradation at > 3.9 V.

If this analysis is carried out on the reference material (PC-LNO), capacity losses of about 1% at high states of charge and 12% due to KH are found. From this result, we conclude that in conventional LNO the first-cycle loss is dominated by KH, and degradation at high potentials plays a minor role, as already reported for NCMs and LNO.[13,34,35] For IE-LNO, on the other hand, a much larger loss at high states of charge of ~5 to 10% is observed, as shown in **Figure 6b**. This loss is slightly increased for the larger particles and is therefore most likely not directly connected to surface degradation, as in this case, an increase with decreasing particle size would be expected.[12] This raises the question of the origin in the bulk material. A possible explanation is layer gliding (note that intragranular cracking has been linked to planar slipping in monolithic particles),[36] with pillaring defects likely preventing the translational movement of NiO_2 slabs and rather causing the formation of stacking faults.[28] Because of the presence of microcracks in the uncycled materials, this hypothesis could not be validated though. By contrast, the KH loss is strongly correlated with particle size and can be decreased from about 23% to almost 2% by decreasing grain size. Regarding KH, IE-LNO seems to be superior to PC-LNO, even if the size of the single-crystalline particles is larger than that of the primary grains, as is the case for IE-LNO-450.[12]

The effects of avoiding $Ni_{Li}^{\bullet}$ defect formation seem to be twofold. On the one hand, diffusion is markedly facilitated, which helps to mitigate KH loss. However, a second loss feature at high states of charge becomes apparent that is usually not observed, as it is weak enough to be ignored in reference LNO. It is well known that defective LNO is unstable at high potentials and tends to form warped layers and release oxygen.[4,13,27] We therefore liken the effects of substitutional point defects to a see-saw, balancing between improved diffusion and deteriorated stability as the $Ni_{Li}^{\bullet}$ concentration approaches 0 mol%.

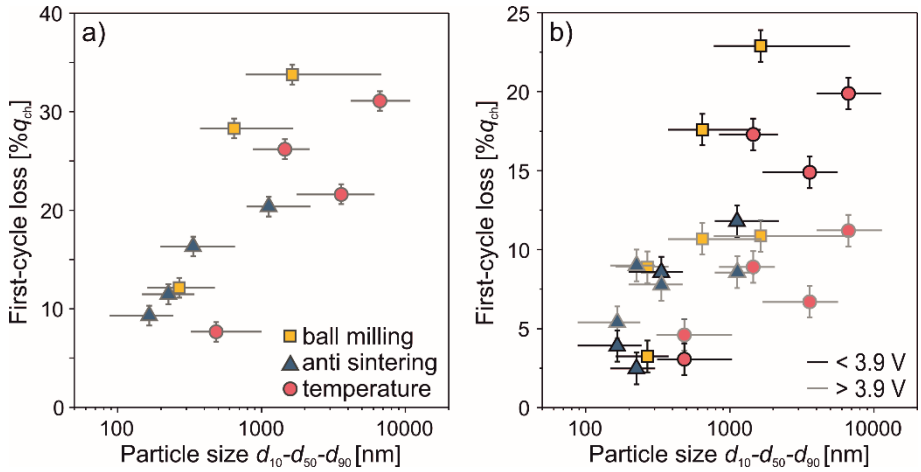

Figure 6. (a) First-cycle capacity loss as a function of particle-size distribution (d_{50} is represented by symbols) for the different IE-LNO samples. (b) Corresponding separation of contributions to the capacity loss above and below 3.9 V vs. Li^+/Li.

Further electrochemical analysis was performed to shed more light on the high-voltage degradation. To confirm that the reported effects originate from the lack of pillaring $Ni_{Li}^{\bullet}$ defects, Mg^{2+} ions were introduced into the lithium site (for mimicking point defects considering the same oxidation state and similar size of Mg^{2+} and Ni^{2+} in octahedral coordination).[37] Firstly, it was attempted to introduce Mg^{2+} during the synthesis of NNO. Here, increasing doping levels are accompanied by decreasing monoclinic distortion (**Figure S6**, Supporting Information), typically present in NNO due to Jahn-Teller distortion of Ni^{3+}. This leads us to the conclusion that Mg^{2+} likely occupies the nickel site in NNO and will maintain its position upon ion exchange. Indeed, even in solid-state syntheses of LNO, Mg^{2+} is found to occupy the lithium and nickel sites in a complex substitution pattern.[38] Hence, with the larger Na^{+} ions being present, Mg^{2+} and similar-sized ions, such as Zn^{2+}, preferentially occupy the transition-metal site.[37] To still introduce Mg^{2+} into the lithium site in IE-LNO, a dual-ion-exchange method was devised. Here, sodium ions are simultaneously replaced with lithium and magnesium ions from a molten salt mixture of lithium and magnesium nitrates. In this example, a salt melt containing 1 mol% magnesium nitrate was prepared and used in the ion exchange of polycrystalline NNO containing 2 mol% tungsten from the anti-sintering approach. The magnesium concentration was found to be 1.49 mol% by ICP-OES (**Table 5**). Compared with IE-LNO-2.0W-PC, this material (referred to as IE-LNO-2.0W-PC-Mg) shows a larger *c*-parameter and cell volume, which is indicative of successful pillaring through dual-ion exchange. It was then used to re-establish the conclusions from the preceding analyses while having the same synthesis history as the unpillared IE-LNO samples.

To fully address the reversible capacity, both the potential window was slightly widened from 3.0-4.3 to 2.9-4.35 V vs. Li^{+}/Li, and the C-rate was lowered to C/20. Under these conditions, initial specific capacities of q_{ch} = 255 and 239 mAh/g_{LNO} and q_{dis} = 222 and 221 mAh/g_{LNO} were achieved with PC-LNO and IE-LNO-2.0W-PC, respectively, corresponding to 13 and 8% first-cycle loss. Because of the polycrystalline morphology, the ion-exchanged LNO is able to deliver similar capacities to conventional LNO despite water washing. This could indicate that a pristine, defect-free LNO would perform even better, but such a material cannot be produced at present. The IE-LNO-2.0W-PC-Mg sample achieved q_{ch} = 223 mAh/g_{LNO} and q_{dis} = 192 mAh/g_{LNO} (14% first-cycle loss). The capacity loss separation was conducted on all three samples, as can be seen in **Figure 7a**, **e**, and **i**. As mentioned previously, PC-LNO shows mainly KH loss, while the IE-LNO materials exhibit contributions from both loss features.

Next, the capacity retention in the regions of interest was examined by galvanostatic cycling in the potential windows of 3.0-3.9 V for the KH loss and 3.9-4.3 V to study the loss associated with high states of charge. The initial voltage profiles and the capacity retentions over 15 cycles of LIB half-cells using the different samples are shown in **Figure 7b**, **c**, **f**, **g**, **j**, and **k**. Cycling below 3.9 V leads to a large initial capacity loss of 17% (with respect to the specific charge capacity delivered between 3.0 and 4.3 V vs. Li^{+}/Li) and then stable behavior for PC-LNO, whereas for both ion-exchanged samples the first-cycle loss is followed by a capacity creep toward higher discharge capacities.

This could point to changes in surface structure upon consecutive cycling, e.g., by removing carbonates. If the highest capacity that is achieved after a few cycles is considered as the true value, overall low capacity losses of about 8 and 10% are observed for IE-LNO-2.0W-PC and IE-LNO-2.0W-PC-Mg, respectively. The latter sample therefore falls in between the two extremes of no pillaring as in IE-LNO-2.0W-PC and $Ni_{Li}^{\bullet}$ defect-pillaring in PC-LNO.

Cycling to high potentials, on the other hand, leads to larger relative first-cycle losses of 24 and 23% for the ion-exchanged material without magnesium and with magnesium, respectively, whereas 4% capacity loss is observed for PC-LNO. All values here are somewhat larger than what is achieved by the separation method used above. This is due to the narrower potential window and large overpotentials for the ion-exchanged samples. This systematically excludes full discharge at 3.9 V and causes an apparently larger first-cycle loss in the high-voltage region. The consecutive cycles show continuous capacity decay to such an extent that 29% of the discharge capacity is lost after 15 cycles in the case of PC-LNO. For IE-LNO-2.0W-PC and IE-LNO-2.0W-PC-Mg, capacity losses of 45 and 7%, respectively, are found. This indicates an increase in long-term stability that is re-introduced into the material by incorporation of Mg^{2+} ions and further suggests that $Ni_{Li}^{\bullet}$-free LNO can even surpass the intrinsic stability of PC-LNO (if stabilized by other means). This result is also corroborated by long-term cycling data (**Figure S7**, Supporting Information), revealing 45, 52, and 60% capacity retention for PC-LNO, IE-LNO-2.0W-PC, and IE-LNO-2.0W-PC-Mg, respectively, after 100 cycles at C/3 rate in the potential window of 2.9-4.35 V vs. Li^{+}/Li.

To gain more insight into the role that diffusion plays in the observed behaviors, galvanostatic intermittent titration technique (GITT) measurements were performed (**Figure S8**, Supporting Information). The extracted open-circuit voltage (OCV) curves are presented in **Figure 7d**, **h**, and **l**. For PC-LNO, almost no difference to cycling at C/20 is observed at high potentials, whereas at the end of discharge a divergence of the curves is apparent. This stands in contrast to IE-LNO-2.0W-PC, for which a large overpotential at high states of charge and striking similarity between the OCV curve and the first-cycle voltage profile in the KH region are observed. This is indicative of facilitated diffusion at the end of discharge and seems to be due to the removal of $Ni_{Li}^{\bullet}$ as physical barrier and the increase in vacancy concentration, which would otherwise be trapped by the point defects. Again, IE-LNO-2.0W-PC-Mg shows an intermediate behavior of these two extremes, further validating substitutional defects to be directly linked to the observed cyclability.

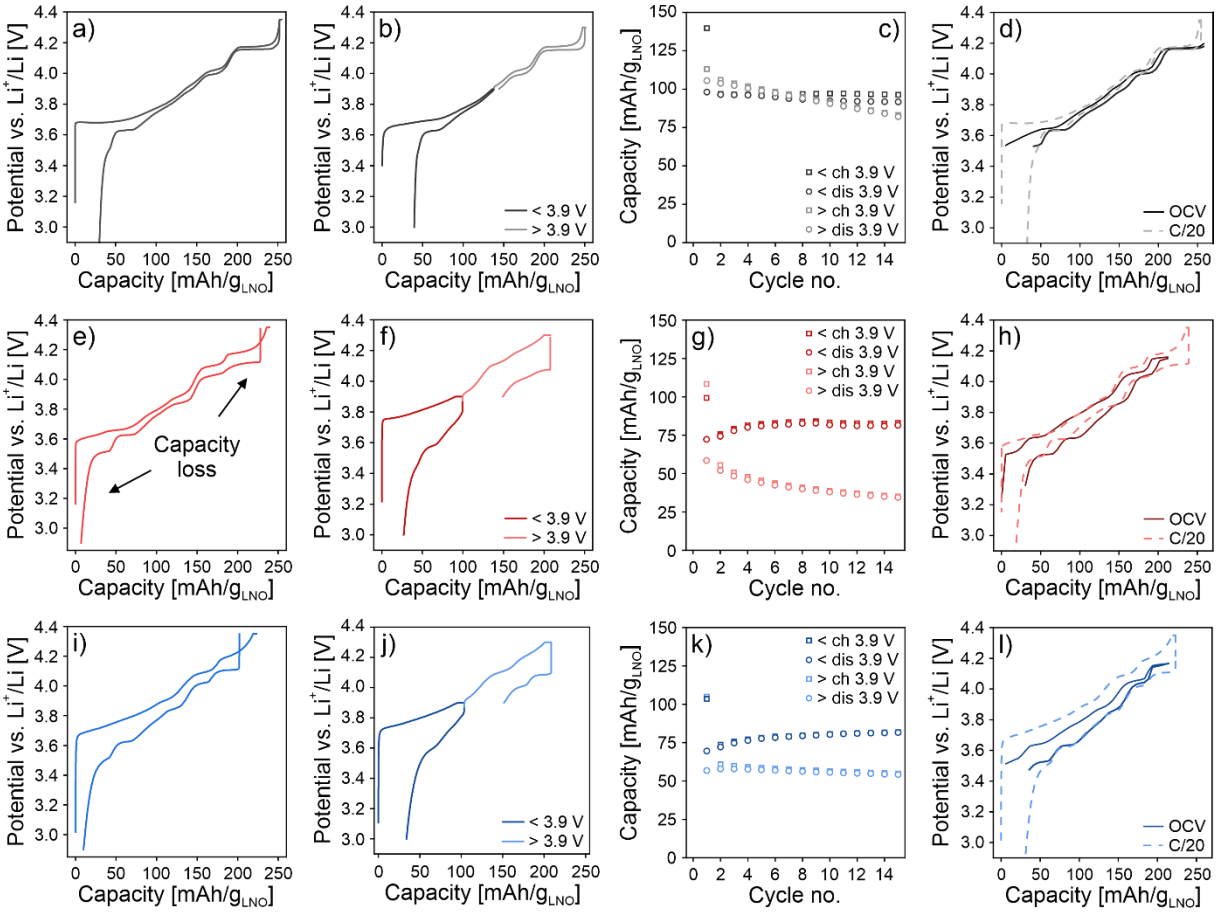

Figure 7. (a,e,i) Aligned first-cycle charge/discharge curves of (a, black) PC-LNO, (e, red) IE-LNO-2.0W-PC, and (I, blue) IE-LNO-2.0W-PC-Mg at C/20 rate (2.9-4.35 V vs. Li^+/Li). (b,f,j) First-cycle charge/discharge curves for cycling in the potential windows of 3.0-3.9 and 3.9-4.3 V vs. Li^+/Li at C/10 rate and (c,g,k) corresponding capacity retentions. (d,h,l) OCV curves (solid line) extracted from GITT measurements performed at an effective rate of C/100 shown together with the as-measured cycling data (dashed line) from panels (a,e,i).

High-Voltage Degradation

The origin of the high-voltage degradation was further analyzed by *ex situ* PXRD measurements and *in situ* gas analysis. Specifically, all three materials were charged to 4.3 V vs. Li^+/Li and kept at this potential until the specific current dropped below 2.0 mA/g_{LNO} (C/100), after which the coin cells were opened in an argon atmosphere and the cathodes probed using PXRD. The corresponding charge curves and experimental patterns are shown in **Figure S7** and **S9** (Supporting Information), respectively. The diffraction data indicate the presence of two phases. The main phase can be assigned to H2, and the other likely corresponds to the collapsed H3 phase. The unpillared material (IE-LNO-2.0W-PC) exhibits the strongest contribution from the H3 phase with 19%, compared to 18% in PC-LNO and 2% in IE-LNO-2.0W-PC-Mg. The phases were further analyzed using the Le Bail method, the results of which are shown in **Table 6**. Both phases are assumed to be hexagonal in nature (*R*−3*m* space group), although it

has been hypothesized previously that O1 stacking can occur in LNO due to layer gliding. The latter was also observed for Ni-rich NCMs, yet the process of O1 formation is apparently very slow.[13,28,36,39,40] This phase is believed to appear below a lithiation degree of 7%, but substitutional defects are expected to prevent gliding at high states of charge.[16,18] Nevertheless, it could be facilitated in IE-LNO due to the lack of $Ni_{Li}^{\bullet}$ defects, which has been predicted to result in lower activation energies for gliding.[41] The presence of the O1 phase, compared to O3, would only be visible by a slight peak broadening, which is inherent in the IE-LNO materials. Therefore, we cannot conclusively discern the two phases. Upon phase transition from H2 to H3, a large anisotropic volume change occurs, leading to a decrease in cell volume by about 6% for PC-LNO. For the ion-exchanged samples, this collapse is much more severe with ~9%. The interlayer spacing is slightly increased for the H3 phase when magnesium is introduced, which is likely a sign of pillaring functionality. Also, the H3 contribution is less pronounced, suggesting that the pillar ions mitigate, to some extent, the phase transformation to the collapsed state. Overall, these results point to an increase in formation of the H3 phase under comparable charging conditions and larger volume variation for the unpillared IE-LNO relative to PC-LNO. If magnesium is introduced into the structure, the interlayer collapse is accompanied by less volume change and the fraction of the H3 phase is significantly reduced.

Table 6. Le Bail refinement results for the charged PC-LNO, IE-LNO-2.0W-PC, and IE-LNO-2.0W-PC-Mg samples.

Sample	R_{wp} [%]	Phase	Fraction [%]	*a* [Å]	*c* [Å]	*V* [Å³]	$\Delta V/V_0$ [%]
PC-LNO	10.5	H2	81.4	2.820(1)	14.400(4)	99.16(1)	−6.2
		H3	18.6	2.818(4)	13.528(30)	93.05(6)	
IE-LNO-2.0W-PC	13.9	H2	80.6	2.819(1)	14.505(2)	99.80(2)	−9.2
		H3	19.4	2.819(2)	13.177(7)	90.66(11)	
IE-LNO-2.0W-PC-Mg	12.6	H2	98.1	2.827(1)	14.476(1)	100.21(2)	−9.0
		H3	1.9	2.824(6)	13.200(12)	91.16(42)	

Finally, differential electrochemical mass spectrometry (DEMS) measurements were performed to examine differences in the gassing behavior, which has also been linked to degradation of LNO at high potentials.[27,42] At the cathode side, CO_2 is the most prominently evolved gas, for which there are three main sources.[42–46] Firstly, surface carbonate impurities formed by exposure of the cathode material to humidity and atmospheric CO_2 decompose under CO_2 evolution, especially in the initial cycle.[44–48] Secondly, oxygen, which subsequently leads to chemical oxidation of the electrolyte, results mostly in CO_2 and, to a lesser extent, O_2 evolution.[45,49,50] Lastly, electrochemical oxidation of the electrolyte also leads to decomposition of the solvent

molecules under CO_2 evolution. However, for ethylene carbonate (EC) as the most common electrolyte solvent, the onset of this decomposition has been determined to be around 4.6 V vs. Li^+/Li.[51–53] **Figure 8a-c** shows the CO_2 evolution profiles for the three materials previously discussed, as obtained via DEMS during cycling of LIB half-cells at C/10 rate between 3.0 V and 4.5 V. **Table S2** (Supporting Information) reports the specific capacities and CO_2 amounts obtained in each cycle and for each material.

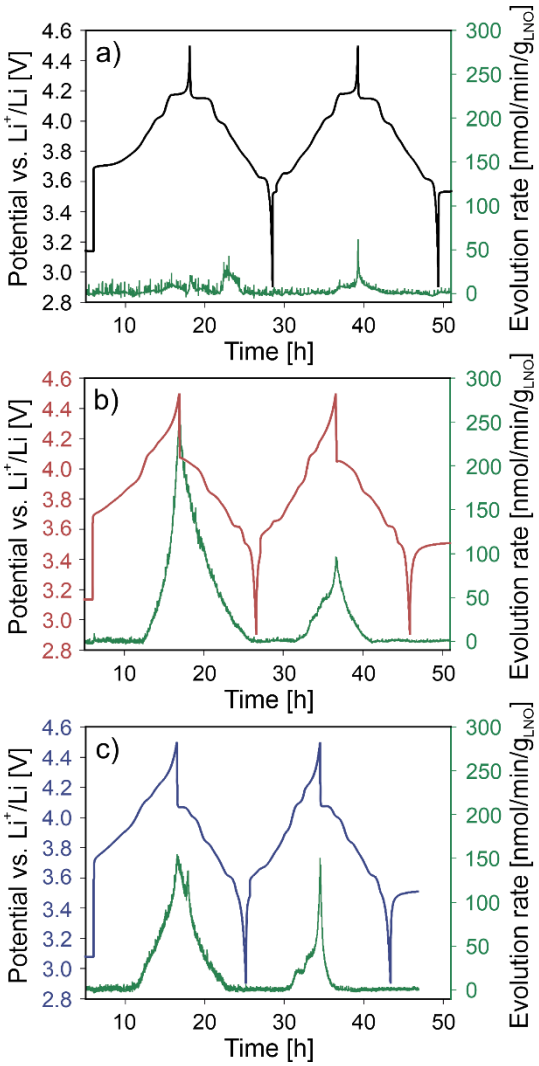

Figure 8. CO_2 evolution as measured by DEMS (3.0-4.5 vs. Li^+/Li, C/10 rate). (a) PC-LNO, (b) IE-LNO-2.0W-PC, and (c) IE-LNO-2.0W-PC-Mg.

Strong differences in CO_2 evolution of the materials are evident and will be discussed in the following. However, while a slightly delayed CO_2 evolution for PC-LNO in the initial cycle is in accordance with previous reports,[27,54,55] the low overall amount and the unusual evolution curve require further considerations. The gas evolution profiles are affected by the use of a rather large volume of electrolyte, which is unfortunately sometimes required for the reliable cycling of DEMS cells in an open-headspace configuration. The reason is that electrolyte is constantly purged out and the cells therefore tend to dry out during the experiment. **Figure S10** (Supporting Information) shows the gas evolution profiles for PC-LNO and IE-LNO-2.0W-PC obtained with a

much lower volume of electrolyte (350 vs. 750 µL). For the IE-LNO-2.0W-PC-Mg sample, no such measurement could be successfully performed. Two main effects can be observed when using less electrolyte. Firstly, the gas evolution profile for IE-LNO-2.0W-PC reveals a higher maximum rate but a narrower peak, resulting in similar total gas amounts after two cycles (82 vs. 88 µmol/g_{LNO}). A likely explanation is the reduced amount of CO_2 dissolved into the electrolyte, leading to less tailing in the evolution peaks. Secondly, a slightly higher gas evolution and a clearer profile are observed for PC-LNO (10 vs. 21 µmol/g_{LNO}). The total CO_2 amount is in good agreement with previous literature reports of NCM and LNO outgassing under consideration of surface purity and upper cutoff potential.[27,31,49,56,57] The detection of additional shoulder peaks or plateaus of gas evolution at lower states of charge or during early discharge, such as for PC-LNO, IE-LNO-2.0W-PC with less electrolyte, and IE-LNO-2.0W-PC-Mg (second cycle), has been previously reported for LNO, although there is still uncertainty whether increased gas evolution is associated with mono- or biphasic delithiation.[27,57] As shown in **Figure S10** (Supporting Information) for PC-LNO, these shoulders mainly correspond to monophasic regions.

The main contribution to outgassing of the materials obtained by ion exchange and the main difference to the gas evolution of PC-LNO obtained via solid-state synthesis is the presence of surface carbonate impurities, likely as remnants of the post-treatment procedure. An onset of CO_2 evolution between 3.8 and 4.0 V, as found in this study, is commonly observed for the decomposition of surface carbonates, yet the contribution of underlying degradation mechanisms is disputed.[42,46,58] The presence of surface carbonates is further confirmed by attenuated total reflection infrared spectroscopy (ATR IR) data collected from the materials (**Figure S7**, Supporting Information).[45,59,60] Unlike IE-LNO-2.0W-PC and IE-LNO-2.0W-PC-Mg, only weak bands are visible for PC-LNO, as expected for a dry-room processed and optimized material. While IE-LNO-2.0W-PC-Mg exhibits the strongest surface carbonate signal, more gas evolution is observed for IE-LNO-2.0W-PC, opening room for discussion of further contributions to gas evolution.

For PC-LNO, most capacity above 4.1 V is obtained during the H2-H3 phase transition, and the cathode is only at high potentials for a relatively short period of time. By contrast, IE-LNO-2.0W-PC and IE-LNO-2.0W-PC-Mg show similar voltage profiles with a less pronounced plateau and a rather linear increase of potential over time during charge above 4.1 V, resulting in a longer time spent at high potentials, accompanied by high gas evolution rates. However, because no significant electrochemical electrolyte oxidation is expected in this potential range, a contribution involving lattice oxygen release (chemical electrolyte oxidation) can be assumed. This could also explain the higher gas evolution seen for IE-LNO-2.0W-PC than IE-LNO-2.0W-PC-Mg, even though the latter likely has more surface carbonates and both materials contain tungsten and are of similar particle size. Considering the lattice collapse in the materials, a possible explanation for higher lattice oxygen release in IE-LNO-2.0W-PC might be the higher H3 phase content and stronger *c*-parameter decrease due to the absence of pillaring ions. If adjacent NiO_2 layers come closer to each other, the formation of oxygen dimers between them may be facilitated, a mechanism suggested

by Kong *et al*. for the (104) facet of LNO and under nickel migration into the lithium layer, i.e., rock-salt-type NiO formation.[61] Yet, Genreith-Schriever *et al*. suggest dimer formation from oxygen atoms of the same layer and under assistance of H_2O, while also pointing to the predominance of the (012) facet and arguing that oxygen, not nickel, is the main redox contributor to LNO capacity.[62] The required peroxo-like intermediates have not been observed (via titration-mass spectrometry) by Kaufman *et al*., which instead link surface crack formation resulting from parasitic reactions with the electrolyte to gas evolution of layered Ni-rich oxide cathodes.[63] This provides further support for the assumption that larger volume variations, due to the absence of pillaring ions, lead to stronger gas evolution. Furthermore, various facets of different stability are found in LNO, and the presence of electrolyte solvent, especially EC, has also been shown to affect the activation energy for lattice oxygen release.[64–66] The lack of pillaring ions is the main difference between the materials and likely to affect lattice oxygen release and nickel reduction, which go hand in hand.

Overall, we find increased oxygen evolution from the ion-exchanged materials as compared to the reference LNO. This is due in part to the presence of surface carbonates. Nevertheless, lattice oxygen release is strongly increased for both materials, with the unpillared system showing the most severe release. These findings underpin the observations made for all size-tailored samples. Upon removing the $Ni_{Li}^{\bullet}$ point defects, the balance between kinetic hindrance and structural stabilization tilts toward improved kinetics and decreased stability accompanied by common signs of degradation, such as oxygen release, which is described by the metaphor of a see-saw.

Conclusions

Sodium to lithium ion exchange is an effective method to prepare high-quality $LiNiO_2$ and represents an ideal platform to study the effect that $Ni_{Li}^{\bullet}$ point defects have on the electrochemical behavior of layered Ni-rich oxide cathode materials. However, small particle (grain) sizes are necessary to ensure full conversion of $NaNiO_2$ to $LiNiO_2$. In this work, three different methods for tailoring of the particle size of $NaNiO_2$ were employed, and the charge-storage properties of the ion-exchanged materials were probed by galvanostatic cycling. For all samples, improvement of lithium diffusion and reduction in first-cycle capacity loss are associated with decreasing particle size, allowing in the case of polycrystalline morphology to lower the irreversible capacity loss on the initial cycle below that of conventional $LiNiO_2$ prepared by solid-state synthesis. Upon removing the $Ni_{Li}^{\bullet}$ point defects, the highly charged state is rendered less stable, leading to electrochemical degradation accompanied by an increase in oxygen evolution from the crystal lattice. The decrease in interlayer spacing is likely accounting for the more severe gassing and thus also for the loss of capacity at high states of charge. However, the formation of stacking faults, due to lack of $Ni_{Li}^{\bullet}$ preventing layer gliding, may occur simultaneously and may lead to intragranular cracking, thereby causing the observed degradation independent of the exposed surface(s). Introduction of Mg^{2+} ions as a substitute for $Ni_{Li}^{\bullet}$ defects can restore some of the stabilization, but

also negatively affects kinetics. We therefore hypothesize a “see-saw effect” of nickel substitutional defects and related pillaring agents, emphasizing the need for an optimal balance between diffusivity and structural stability to optimize first-cycle efficiency and battery performance.

Experimental Section

Synthesis of $NaNiO_2$. $NaNiO_2$ was prepared by solid-state reaction from $Ni(OH)_2$ (d_{50} = 4 µm, BASF SE) or NiO nanoparticles (d_{50} = 50 nm, BASF SE) and NaOH (Sigma-Aldrich) or Na_2O_2 (Sigma-Aldrich), and optionally ammonium paratungstate (Sigma-Aldrich) as indicated. The reactants were homogenized in a laboratory blender (Kinematica) under an Ar atmosphere for 5 min with 10 mol% excess of $NaOH/Na_2O_2$ [i.e., *n*(Ni):*n*(Na) = 1:1.1]. The precursor mixtures were then heated in an Al_2O_3 crucible under oxygen flow (~2 volume exchanges per h) in a tube furnace (Nabertherm P330) at 300 °C for 10 h with 3 K/min heating and cooling rates. After cooling, the reactant mixtures were homogenized again for 5 min, and in one instance, ammonium paratungstate was added to produce polycrystalline material. The resulting mixtures were transferred to an Al_2O_3 crucible for calcination at 450-700 °C for 12 h under oxygen flow (~2 volume exchanges per h) and with 3 K/min heating and cooling rates. The products were sieved using a 32 µm steel mesh.

Synthesis of Mg-doped $NaNiO_2$. It was attempted to dope magnesium into the $NaNiO_2$ structure by addition of $Mg(OH)_2$ nanoparticles (10 nm, US Research Nanomaterials Inc.) to the synthesis outlined for $NaNiO_2$ above, with the amounts indicated in the main text and Figure S6.

Synthesis of reference $LiNiO_2$. Reference (polycrystalline) $LiNiO_2$ was prepared by solid-state reaction from $Ni(OH)_2$ (d_{50} = 14 µm, BASF SE) and $LiOH{\cdot}H_2O$ (10-20 µm, BASF SE). The reactants were dry mixed in a blender (Kinematica) under an Ar atmosphere for 5 min in the required ratios with 1 mol% excess of $LiOH{\cdot}H_2O$. The precursor mixture was then calcined in an Al_2O_3 crucible under oxygen flow (~2 volume exchanges per h) in a tube furnace (Nabertherm P330) at 700 °C for 8 h with 3 K/min heating and cooling rates and with a pre-heating step at 400 °C for 4 h. The product was sieved using a 32 µm steel mesh.

Ball milling of $NaNiO_2$. $NaNiO_2$ was milled in a planetary ball mill (Fritsch) with a 20:1 ball-to-powder weight ratio using 2 mm ZrO_2 balls at the indicated rotational speed of 300-600 rpm for 10 min. The product was directly used for ion exchange.

Synthesis of Mg-Containing $LiNO_3$. A mixture of 90 mol% $LiNO_3$ and 10 mol% $Mg(NO_3)_2$ (Sigma-Aldrich) was liquefied at 350 °C, followed by quenching to room temperature. Subsequently, it was homogenized and used as a dry mixture with $LiNO_3$ in a ratio of 1:10 Mg/Li:Li.

Ion-Exchange Protocol. 1 g $NaNiO_2$ and 1 g $LiNO_3$ (Sigma-Aldrich) or 1 mol% Mg-containing $LiNO_3$ were mixed in a mortar and pestle and filled into an Al_2O_3 crucible.

The powder mixtures were heated at 300 °C for 6 h and left to cool to room temperature. A PTFE-coated magnetic stir bar and 50 mL LiOH solution (pH = 12.5, 0.025 M) were used to dissolve the remaining nitrate salt, and the resulting materials were washed with 50 mL LiOH solution, 10 mL ethanol, and 10 mL acetone. The products were dried in a vacuum at 65 °C and sieved using a 32 µm steel mesh.

Electrochemical Testing. Electrode tapes were prepared by casting an N-methyl-pyrrolidone (NMP)-based slurry with 96 wt% cathode material, 3 wt% Super C65 carbon additive, and 3 wt% polyvinylidene difluoride binder (Solef 5130, Solvay) onto 0.03 mm Al foil as current collector. The slurry was prepared freshly by combining all constituents with 20 wt% additional NMP in a planetary mixer (ARE250, Thinky) and stirring using a two-step program (3 min at 2000 rpm, 3 min at 400 rpm). The slurry was spread at a casting thickness of 140 µm and at a rate of 5 mm/s using an Erichsen Coatmaster 510 coating machine with a stainless-steel blade. The obtained tapes were dried overnight in a vacuum at 120 °C and calendared at 14 N/mm (Sumet Messtechnik). Individual circular cathodes of 13 mm diameter were cut, and LIB half-cells containing LP57 electrolyte (1 M $LiPF_6$ in a mixture of ethylene carbonate and ethyl methyl carbonate [3:7 ratio]), a GF/D separator, and a Li-metal anode were assembled in an Ar-glovebox.

SEM. Morphological and compositional insights into the as-prepared samples were obtained from field-emission SEM and EDS using a LEO-1530 microscope (Carl Zeiss AG).

FIB. Electron-transparent specimens for TEM investigation were prepared by the lift-out technique using an FEI Strata 400 S dual-beam system. Gallium ion beam induced sample damage and amorphization were minimized by stepwise reduction of the acceleration voltage, from 30 to 2 keV, during final thinning of the lamella. Specimen preparation was immediately followed by TEM investigation to reduce possible oxidation during sample storage.

(S)TEM. (S)TEM images were acquired at 300 keV using a probe aberration-corrected Thermo Fisher Scientific (TFS) Themis Z microscope. EDS maps were collected with a Super-X EDX detector.

ICP-OES. The composition of the products was determined by ICP-OES using a Thermo Fisher Scientific ICAP 7600 DUO. To this end, powder samples were dissolved in an acid digester in a graphite furnace. Mass fractions were obtained from three independent measurements for each sample. About 10 mg material of interest was dissolved in 6 mL hydrochloric acid and 2 mL nitric acid at 353 K for 4 h. The digested samples were diluted, and analysis of the elements was conducted with four different calibration solutions and an internal standard (Sc). The range of the calibration solutions did not exceed a decade. Two or three wavelengths of the elements were used for analysis. The oxygen content was analyzed by carrier gas hot extraction using a commercial oxygen/nitrogen analyzer TC600 (LECO). The oxygen content was calibrated with the certified standard KED 1025, a steel powder from ALPHA. The standards and samples were weighed with a mass in the range 1-2 mg, in addition to

5 mg graphite, in Sn crucibles (9-10 mm) and wrapped. Together with a Sn pellet, the wrapped samples were placed in a Ni crucible and loaded in an outgassed double-graphite crucible. Evolving CO_2 and CO were swept out by He carrier gas and measured by infrared detectors.

Capillary PXRD. PXRD patterns were collected on a STADI P (STOE) diffractometer in Debye-Scherrer geometry with monochromatic Mo $K\alpha_1$ radiation (λ = 0.7093 Å, 50 kV, 40 mA) and a Mythen 1K detector (Dectris). The diffraction data sets were analyzed using TOPAS Academic v7. LeBail fitting was done first, in which background correction was applied by a set of Chebyshev polynomials (10 terms), and lattice parameters, zero-shift, axial divergence, and crystallite size were extracted as Gaussian and Lorentzian contributions. The phenomenological model by Stephens was used to describe *hkl*-dependent microstrain.[67] During Rietveld refinement, the parameters from LeBail fitting were first fixed, and the oxygen coordinate(s) z_O ($LiNiO_2$) and z_{O_1} and z_{O_2} ($NaNiO_2$), site occupancies, and Debye-Waller factors were refined while applying an absorption correction. Lastly, all parameters were refined in parallel until convergence was achieved. The confidence intervals were three times the estimated standard deviations as obtained from TOPAS Academic.

ATR-IR Spectroscopy. Spectra were measured in an Ar-glovebox using an ALPHA FT-IR spectrometer equipped with an Eco ATR sampling module. The data were Fourier transformed using the OPUS software (Bruker) and background subtracted with Origin Pro 2021.

DEMS. Cells consisting of a 30 mm diameter cathode with a 4 mm hole in the center, a 40 mm diameter GF/D separator, a 32 mm Li-metal anode, and 750 µL LP57 electrolyte were assembled in a customized housing. In a variation, only 350 µL electrolyte was used. The cells were cycled at 0.1C rate between 3.0 and 4.5 V vs. Li^+/Li for two cycles, while a stream of He carrier gas (2.5 mL/min, purity 6.0) was constantly passed through. After passing a cold trap (−30 °C) to condensate extracted electrolyte solvent, the gas mixture was analyzed by a mass spectrometer (GSD320, Pfeiffer Vacuum GmbH). A calibration curve was obtained from measuring various dilutions of a gas of known composition. A more detailed description of the setup and method is available in the literature.[42,68,69]

Associated Content

Supporting Information

PXRD patterns and refinement plots/results; electrochemical testing data (including cycling and GITT), TEM/EDS analysis, ATR-IR spectra, and DEMS results.

Notes

The authors declare no competing financial interest.

Acknowledgments

This work was partially supported by BASF SE. The authors are grateful to the Federal Ministry of Education and Research (Bundesministerium für Bildung und Forschung, BMBF) for funding within the project UNIKAM (03XP0484B). Thomas Bergfeldt is acknowledged for conducting the ICP-OES measurements and Philipp Müller for TEM analysis of NNO. The authors also thank Damian Goonetilleke and Nikolai Bartnick for experimental support. The authors acknowledge the support from the Karlsruhe Nano Micro Facility (KNMFi, www.knmf.kit.edu), a Helmholtz research infrastructure at Karlsruhe Institute of Technology (KIT, www.kit.edu).

References

(1) Xiao, J.; Chernova, N. A.; Whittingham, M. S. Layered Mixed Transition Metal Oxide Cathodes with Reduced Cobalt Content for Lithium Ion Batteries. *Chem. Mater.* **2008**, *20*, 7454–7464.

(2) Hoang, K.; Johannes, M. Defect Physics and Chemistry in Layered Mixed Transition Metal Oxide Cathode Materials: (Ni,Co,Mn) vs (Ni,Co,Al). *Chem. Mater.* **2016**, *28*, 1325–1334.

(3) Chernova, N. A.; Nolis, G. M.; Omenya, F. O.; Zhou, H.; Li, Z.; Whittingham, M. S. What Can We Learn about Battery Materials from Their Magnetic Properties? *J. Mater. Chem.* **2011**, *21*, 9865–9875.

(4) Bianchini, M.; Roca-Ayats, M.; Hartmann, P.; Brezesinski, T.; Janek, J. There and Back Again—The Journey of $LiNiO_2$ as a Cathode Active Material. *Angew. Chem., Int. Ed.* **2019**, *58*, 10434–10458.

(5) Kanno, R.; Kubo, H.; Kawamoto, Y.; Kamiyama, T.; Izumi, F.; Takeda, Y.; Takano, M. Phase Relationship and Lithium Deintercalation in Lithium Nickel Oxides. *J. Solid State Chem.* **1994**, *110*, 216–225.

(6) Li, W.; Reimers, J. N.; Dahn, J. R. Crystal Structure of $Li_xNi_{2-x}O_2$ and a Lattice-Gas Model for the Order-Disorder Transition. *Phys. Rev. B* **1992**, *46*, 3236–3246.

(7) Goonetilleke, D.; Schwarz, B.; Li, H.; Fauth, F.; Suard, E.; Mangold, S.; Indris, S.; Brezesinski, T.; Bianchini, M.; Weber, D. Stoichiometry Matters: Correlation between Antisite Defects, Microstructure and Magnetic Behavior in the Cathode Material $Li_{1-z}Ni_{1+z}O_2$. *J. Mater. Chem. A* **2023**, *11*, 13468–13482.

(8) Pokle, A.; Weber, D.; Bianchini, M.; Janek, J.; Volz, K. Probing the $Ni(OH)_2$ Precursor for $LiNiO_2$ at the Atomic Scale: Insights into the Origin of Structural Defect in a Layered Cathode Active Material. *Small* **2023**, *19*, 2205508.

(9) Bianchini, M.; Fauth, F.; Hartmann, P.; Brezesinski, T.; Janek, J. An In Situ Structural Study on the Synthesis and Decomposition of $LiNiO_2$. *J. Mater. Chem. A* **2020**, *8*, 1808–1820.

(10) Wei, H.; Tang, L.; Huang, Y.; Wang, Z.; Luo, Y.; He, Z.; Yan, C.; Mao, J.; Dai, K.; Zheng, J. Comprehensive Understanding of Li/Ni Intermixing in Layered Transition Metal Oxides. *Mater. Today* **2021**, *51*, 365–392.

(11) Kurzhals, P.; Riewald, F.; Bianchini, M.; Sommer, H.; Gasteiger, H. A.; Janek, J. The $LiNiO_2$ Cathode Active Material: A Comprehensive Study of Calcination Conditions and Their Correlation with Physicochemical Properties. Part I. Structural Chemistry. *J. Electrochem. Soc.* **2021**, *168*, 110518.

(12) Riewald, F.; Kurzhals, P.; Bianchini, M.; Sommer, H.; Janek, J.; Gasteiger, H. A. The $LiNiO_2$ Cathode Active Material: A Comprehensive Study of Calcination Conditions and Their Correlation with Physicochemical Properties Part II. Morphology. *J. Electrochem. Soc.* **2022**, *169*, 020529.

(13) Quisbert, E. B.; Fauth, F.; Abakumov, A. M.; Blangero, M.; Guignard, M.; Delmas, C. Understanding the High Voltage Behavior of $LiNiO_2$ Through the Electrochemical Properties of the Surface Layer. *Small* **2023**, *19*, 2300616.

(14) Karger, L.; Weber, D.; Goonetilleke, D.; Mazilkin, A.; Li, H.; Zhang, R.; Ma, Y.; Indris, S.; Kondrakov, A.; Janek, J.; Brezesinski, T. Low-Temperature Ion Exchange Synthesis of Layered $LiNiO_2$ Single Crystals with High Ordering. *Chem. Mater.* **2023**, *35*, 648–657.

(15) Peres, J. P.; Delmas, C.; Rougier, A.; Broussely, M.; Perton, F.; Biensan, P.; Willmann, P. The Relationship between the Composition of Lithium Nickel Oxide and the Loss of Reversibility during the First Cycle. *J. Phys. Chem. Solids* **1996**, *57*, 1057–1060.

(16) Croguennec, L.; Pouillerie, C.; Mansour, A. N.; Delmas, C. Structural Characterisation of the Highly Deintercalated $Li_xNi_{1.02}O_2$ Phases (with $x \leq 0.30$). *J. Mater. Chem.* **2001**, *11*, 131–141.

(17) Tarascon, J. M.; Vaughan, G.; Chabre, Y.; Seguin, L.; Anne, M.; Strobel, P.; Amatucci, G. In Situ Structural and Electrochemical Study of $Ni_{1-x}Co_xO_2$ Metastable Oxides Prepared by Soft Chemistry. *J. Solid State Chem.* **1999**, *147*, 410–420.

(18) Croguennec, L.; Pouillerie, C.; Delmas, C. Structural Characterisation of New Metastable NiO_2 Phases. *Solid State Ionics* **2000**, *135*, 259–266.

(19) Arai, H.; Okada, S.; Ohtsuka, H.; Ichimura, M.; Yamaki, J. Characterization and Cathode Performance of $Li_{1-x}Ni_{1+x}O_2$ Prepared with the Excess Lithium Method. *Solid State Ionics* **1995**, *80*, 261–269.

(20) Delmas, C.; Pérès, J. P.; Rougier, A.; Demourgues, A.; Weill, F.; Chadwick, A.; Broussely, M.; Perton, F.; Biensan, Ph.; Willmann, P. On the Behavior of the Li_xNiO_2 System: An Electrochemical and Structural Overview. *J. Power Sources* **1997**, *68*, 120–125.

(21) Bianchi, V.; Bach, S.; Belhomme, C.; Farcy, J.; Pereira-Ramos, J. P.; Caurant, D.; Baffier, N.; Willmann, P. Electrochemical Investigation of the Li Insertion-

Extraction Reaction as a Function of Lithium Deficiency in $Li_{1-x}Ni_{1+x}O_2$. *Electrochim. Acta* **2001**, *46*, 999–1011.

(22) Xu, Z.; Wang, Z.; Tan, X.; Guo, H.; Peng, W.; Li, X.; Wang, J.; Yan, G. Correlating Morphological and Structural Evolution with the Electrochemical Performance of Nickel-Rich Cathode Materials: From Polycrystal to Single Crystal. *J. Electrochem. Soc.* **2022**, *169*, 090520.

(23) Sicolo, S.; Sadowski, M.; Vettori, K.; Bianchini, M.; Janek, J. Off-Stoichiometry, Vacancy Trapping and Pseudo-Irreversible First-Cycle Capacity in $LiNiO_2$. ChemRxiv (Theoretical and Computational Chemistry) **2023**, 10.26434/chemrxiv-2023-hkmsn_v3, (accessed 31.09.2023).

(24) van den Bergh, W.; Karger, L.; Murugan, S.; Janek, J.; Kondrakov, A.; Brezesinski, T. Single Crystal Layered Oxide Cathodes: The Relationship between Particle Size, Rate Capability, and Stability. *ChemElectroChem* **2023**, *10*, 202300165.

(25) Rougier, A.; Gravereau, P.; Delmas, C. Optimization of the Composition of the $Li_{1-z}Ni_{1+z}O_2$ Electrode Materials: Structural, Magnetic, and Electrochemical Studies. *J. Electrochem. Soc.* **1996**, *143*, 1168–1175.

(26) Li, H.; Zhang, N.; Li, J.; Dahn, J. R. Updating the Structure and Electrochemistry of Li_xNiO_2 for $0 \leq x \leq 1$. *J. Electrochem. Soc.* **2018**, *165*, A2985–A2993.

(27) de Biasi, L.; Schiele, A.; Roca-Ayats, M.; Garcia, G.; Brezesinski, T.; Hartmann, P.; Janek, J. Phase Transformation Behavior and Stability of $LiNiO_2$ Cathode Material for Li-Ion Batteries Obtained from In Situ Gas Analysis and Operando X-Ray Diffraction. *ChemSusChem* **2019**, *12*, 2240–2250.

(28) Mock, M.; Bianchini, M.; Fauth, F.; Albe, K.; Sicolo, S. Atomistic Understanding of the $LiNiO_2$–NiO_2 Phase Diagram from Experimentally Guided Lattice Models. *J. Mater. Chem. A* **2021**, *9*, 14928–14940.

(29) Liu, A.; Phattharasupakun, N.; Cormier, M. M. E.; Zsoldos, E.; Zhang, N.; lyle, E.; Arab, P.; Sawangphruk, M.; Dahn, J. R. Factors That Affect Capacity in the Low Voltage Kinetic Hindrance Region of Ni-Rich Positive Electrode Materials and Diffusion Measurements from a Reinvented Approach. *J. Electrochem. Soc.* **2021**, *168*, 070503.

(30) Rueß, R.; Gomboso, D.; Ulherr, M.; Trevisanello, E.; Ma, Y.; Kondrakov, A.; Brezesinski, T.; Janek, J. Single-Crystalline $LiNiO_2$ as High-Capacity Cathode Active Material for Solid-State Lithium-Ion Batteries. *J. Electrochem. Soc.* **2023**, *170*, 020533.

(31) Oswald, S.; Pritzl, D.; Wetjen, M.; Gasteiger, H. A. Novel Method for Monitoring the Electrochemical Capacitance by In Situ Impedance Spectroscopy as Indicator for Particle Cracking of Nickel-Rich NCMs: Part II. Effect of Oxygen Release Dependent on Particle Morphology. *J. Electrochem. Soc.* **2021**, *168*, 120501.

(32) Pritzl, D.; Teufl, T.; Freiberg, A. T. S.; Strehle, B.; Sicklinger, J.; Sommer, H.; Hartmann, P.; Gasteiger, H. A. Editors' Choice—Washing of Nickel-Rich Cathode Materials for Lithium-Ion Batteries: Towards a Mechanistic Understanding. *J. Electrochem. Soc.* **2019**, *166*, A4056–A4066.

(33) Goonetilleke, D.; Mazilkin, A.; Weber, D.; Ma, Y.; Fauth, F.; Janek, J.; Brezesinski, T.; Bianchini, M. Single Step Synthesis of W-Modified $LiNiO_2$ Using an Ammonium Tungstate Flux. *J. Mater. Chem. A* **2022**,*10*, 7841–7855.

(34) Kasnatscheew, J.; Evertz, M.; Streipert, B.; Wagner, R.; Klöpsch, R.; Vortmann, B.; Hahn, H.; Nowak, S.; Amereller, M.; Gentschev, A.-C.; Lamp, P.; Winter, M. The Truth about the 1st Cycle Coulombic Efficiency of $LiNi_{1/3}Co_{1/3}Mn_{1/3}O_2$ (NCM) Cathodes. *Phys. Chem. Chem. Phys.* **2016**, *18*, 3956–3965.

(35) Bae, C.; Dupre, N.; Kang, B. Further Improving Coulombic Efficiency and Discharge Capacity in $LiNiO_2$ Material by Activating Sluggish ~3.5 V Discharge Reaction. *ACS Appl. Mater. Interfaces* **2021**, *13*, 23760–23770.

(36) Bi, Y.; Tao, J.; Wu, Y.; Li, L.; Xu, Y.; Hu, E.; Wu, B.; Hu, J.; Wang, C.; Zhang, J.-G.; Qi, Y.; Xiao, J. Reversible Planar Gliding and Microcracking in a Single-Crystalline Ni-Rich Cathode. *Science* **2020**, *370*, 1313–1318.

(37) Shannon, R. D. Revised Effective Ionic Radii and Systematic Studies of Interatomic Distances in Halides and Chalcogenides. *Acta Cryst.* **1976**, *A32*, 751–767.

(38) Weber, D.; Lin, J.; Pokle, A.; Volz, K.; Janek, J.; Brezesinski, T.; Bianchini, M. Tracing Low Amounts of Mg in the Doped Cathode Active Material $LiNiO_2$. *J. Electrochem. Soc.* **2022**, *169*, 030540.

(39) Ruff, Z.; Coates, C. S.; Märker, K.; Mahadevegowda, A.; Xu, C.; Penrod, M. E.; Ducati, C.; Grey, C. P. O3 to O1 Phase Transitions in Highly Delithiated NMC811 at Elevated Temperatures. *Chem. Mater.* **2023**, *35*, 4979–4987.

(40) Wang, C.; Zhang, R.; Kisslinger, K.; Xin, H. L. Atomic-Scale Observation of O1 Faulted Phase-Induced Deactivation of $LiNiO_2$ at High Voltage. *Nano Lett.* **2021**, *21*, 3657–3663.

(41) Sadowski, M.; Koch, L.; Albe, K.; Sicolo, S. Planar Gliding and Vacancy Condensation: The Role of Dislocations in the Chemomechanical Degradation of Layered Transition-Metal Oxides. *Chem. Mater.* **2023**, *35*, 584–594.

(42) Dreyer, S. L.; Kondrakov, A.; Janek, J.; Brezesinski, T. In Situ Analysis of Gas Evolution in Liquid- and Solid-Electrolyte-Based Batteries with Current and Next-Generation Cathode Materials. *J. Mater. Res.* **2022**, *37*, 3146–3168.

(43) Salomez, B.; Grugeon, S.; Armand, M.; Tran-Van, P.; Laruelle, S. Review—Gassing Mechanisms in Lithium-Ion Battery. *J. Electrochem. Soc.* **2023**, *170*, 050537.

(44) Renfrew, S. E.; McCloskey, B. D. Residual Lithium Carbonate Predominantly Accounts for First Cycle CO_2 and CO Outgassing of Li-Stoichiometric and Li-

Rich Layered Transition-Metal Oxides. *J. Am. Chem. Soc.* **2017**, *139*, 17853–17860.

(45) Hatsukade, T.; Schiele, A.; Hartmann, P.; Brezesinski, T.; Janek, J. Origin of Carbon Dioxide Evolved during Cycling of Nickel-Rich Layered NCM Cathodes. *ACS Appl. Mater. Interfaces* **2018**, *10*, 38892–38899.

(46) Freiberg, A. T. S.; Sicklinger, J.; Solchenbach, S.; Gasteiger, H. A. Li_2CO_3 Decomposition in Li-Ion Batteries Induced by the Electrochemical Oxidation of the Electrolyte and of Electrolyte Impurities. *Electrochim. Acta* **2020**, *346*, 136271.

(47) Sicklinger, J.; Metzger, M.; Beyer, H.; Pritzl, D.; Gasteiger, H. A. Ambient Storage Derived Surface Contamination of NCM811 and NCM111: Performance Implications and Mitigation Strategies. *J. Electrochem. Soc.* **2019**, *166*, A2322–A2335.

(48) Fang, Z.; Confer, M. P.; Wang, Y.; Wang, Q.; Kunz, M. R.; Dufek, E. J.; Liaw, B.; Klein, T. M.; Dixon, D. A.; Fushimi, R. Formation of Surface Impurities on Lithium–Nickel–Manganese–Cobalt Oxides in the Presence of CO_2 and H_2O. *J. Am. Chem. Soc.* **2021**, *143*, 10261–10274.

(49) Streich, D.; Erk, C.; Guéguen, A.; Müller, P.; Chesneau, F.-F.; Berg, E. J. Operando Monitoring of Early Ni-Mediated Surface Reconstruction in Layered Lithiated Ni–Co–Mn Oxides. *J. Phys. Chem. C* **2017**, *121*, 13481–13486.

(50) Wandt, J.; Freiberg, A. T. S.; Ogrodnik, A.; Gasteiger, H. A. Singlet Oxygen Evolution from Layered Transition Metal Oxide Cathode Materials and Its Implications for Lithium-Ion Batteries. *Mater. Today* **2018**, *21*, 825–833.

(51) Metzger, M.; Walke, P.; Solchenbach, S.; Salitra, G.; Aurbach, D.; Gasteiger, H. A. Evaluating the High-Voltage Stability of Conductive Carbon and Ethylene Carbonate with Various Lithium Salts. *J. Electrochem. Soc.* **2020**, *167*, 160522.

(52) Metzger, M.; Marino, C.; Sicklinger, J.; Haering, D.; Gasteiger, H. A. Anodic Oxidation of Conductive Carbon and Ethylene Carbonate in High-Voltage Li-Ion Batteries Quantified by On-Line Electrochemical Mass Spectrometry. *J. Electrochem. Soc.* **2015**, *162*, A1123–A1134.

(53) Jung, R.; Metzger, M.; Maglia, F.; Stinner, C.; Gasteiger, H. A. Chemical versus Electrochemical Electrolyte Oxidation on NMC111, NMC622, NMC811, LNMO, and Conductive Carbon. *J. Phys. Chem. Lett.* **2017**, *8*, 4820–4825.

(54) Misiewicz, C.; Lundström, R.; Ahmed, I.; Lacey, M. J.; Brant, W. R.; Berg, E. J. Online Electrochemical Mass Spectrometry on Large-Format Li-Ion Cells. *J. Power Sources* **2023**, *554*, 232318.

(55) Lundström, R.; Berg, E. J. Design and Validation of an Online Partial and Total Pressure Measurement System for Li-Ion Cells. *J. Power Sources* **2021**, *485*, 229347.

(56) Dreyer, S. L.; Kurzhals, P.; Seiffert, S. B.; Müller, P.; Kondrakov, A.; Brezesinski,

T.; Janek, J. The Effect of Doping Process Route on $LiNiO_2$ Cathode Material Properties. *J. Electrochem. Soc.* **2023**, *170*, 060530.

(57) Oswald, S.; Gasteiger, H. A. The Structural Stability Limit of Layered Lithium Transition Metal Oxides Due to Oxygen Release at High State of Charge and Its Dependence on the Nickel Content. *J. Electrochem. Soc.* **2023**, *170*, 030506.

(58) Kaufman, L. A.; McCloskey, B. D. Surface Lithium Carbonate Influences Electrolyte Degradation via Reactive Oxygen Attack in Lithium-Excess Cathode Materials. *Chem. Mater.* **2021**, *33*, 4170–4176.

(59) Kim, A.-Y.; Strauss, F.; Bartsch, T.; Teo, J. H.; Hatsukade, T.; Mazilkin, A.; Janek, J.; Hartmann, P.; Brezesinski, T. Stabilizing Effect of a Hybrid Surface Coating on a Ni-Rich NCM Cathode Material in All-Solid-State Batteries. *Chem. Mater.* **2019**, *31*, 9664–9672.

(60) Busca, G.; Lorenzelli, V. Infrared Spectroscopic Identification of Species Arising from Reactive Adsorption of Carbon Oxides on Metal Oxide Surfaces. *Mater. Chem.* **1982**, *7*, 89–126.

(61) Kong, F.; Liang, C.; Wang, L.; Zheng, Y.; Perananthan, S.; Longo, R. C.; Ferraris, J. P.; Kim, M.; Cho, K. Kinetic Stability of Bulk $LiNiO_2$ and Surface Degradation by Oxygen Evolution in $LiNiO_2$-Based Cathode Materials. *Adv. Energy Mater.* **2019**, *9*, 1802586.

(62) Genreith-Schriever, A. R.; Banerjee, H.; Menon, A. S.; Bassey, E. N.; Piper, L. F. J.; Grey, C. P.; Morris, A. J. Oxygen Hole Formation Controls Stability in $LiNiO_2$ Cathodes. *Joule* **2023**, *7*, 1623–1640.

(63) Kaufman, L. A.; Huang, T.-Y.; Lee, D.; McCloskey, B. D. Particle Surface Cracking Is Correlated with Gas Evolution in High-Ni Li-Ion Cathode Materials. *ACS Appl. Mater. Interfaces* **2022**, *14*, 39959–39964.

(64) Su, C.-C.; He, M.; Amine, R.; Chen, Z.; Yu, Z.; Rojas, T.; Cheng, L.; Ngo, A. T.; Amine, K. Unveiling Decaying Mechanism through Quantitative Structure-Activity Relationship in Electrolytes for Lithium-Ion Batteries. *Nano Energy* **2021**, *83*, 105843.

(65) Garcia, J. C.; Bareño, J.; Yan, J.; Chen, G.; Hauser, A.; Croy, J. R.; Iddir, H. Surface Structure, Morphology, and Stability of $Li(Ni_{1/3}Mn_{1/3}Co_{1/3})O_2$ Cathode Material. *J. Phys. Chem. C* **2017**, *121*, 8290–8299.

(66) Dose, W. M.; Temprano, I.; Allen, J. P.; Björklund, E.; O'Keefe, C. A.; Li, W.; Mehdi, B. L.; Weatherup, R. S.; De Volder, M. F. L.; Grey, C. P. Electrolyte Reactivity at the Charged Ni-Rich Cathode Interface and Degradation in Li-Ion Batteries. *ACS Appl. Mater. Interfaces* **2022**, *14*, 13206–13222.

(67) Stephens, P. W. Phenomenological Model of Anisotropic Peak Broadening in Powder Diffraction. *J. Appl. Cryst.* **1999**, *32*, 281–289.

(68) Berkes, B. B.; Jozwiuk, A.; Sommer, H.; Brezesinski, T.; Janek, J. Simultaneous Acquisition of Differential Electrochemical Mass Spectrometry and Infrared

Spectroscopy Data for In Situ Characterization of Gas Evolution Reactions in Lithium-Ion Batteries. *Electrochem. Commun.* **2015**, *60*, 64–69.

(69) Berkes, B. B.; Jozwiuk, A.; Vračar, M.; Sommer, H.; Brezesinski, T.; Janek, J. Online Continuous Flow Differential Electrochemical Mass Spectrometry with a Realistic Battery Setup for High-Precision, Long-Term Cycling Tests. *Anal. Chem.* **2015**, *87*, 5878–5883.

TOC Image